# Analysis of capillary water imbibition in sandstone via a combination of nuclear magnetic resonance imaging and numerical DEM modeling

Teng-Fei Fu[a], Tao Xu[a*], Michael J. Heap[b], Philip G. Meredith[c], Tian-hong Yang[a], Thomas M. Mitchell[c], Yoshitaka Nara[d]

[a] Center for Rock Instability and Seismicity Research, Northeastern University, Shenyang, 110819, China

[b]Université de Strasbourg, CNRS, ENGEES, Institut Terre et Environnement de Strasbourg, UMR 7063, 5 rue René Descartes, Strasbourg F-67084, France

[c]Rock & Ice Physics Laboratory, Department of Earth Sciences, University College London, Gower Street, London WC1E6BT, UK

[d]Department of Civil and Earth Resources Engineering, Graduate School of Engineering, Kyoto University, Kyoto Daigaku Katsura, Nishikyo-ku, Kyoto 615-8540, Japan

*Corresponding author: xutao@mail.neu.edu.cn

**Abstract**

The physics of water imbibition into initially unsaturated sandstone is critical to the understanding of displacement processes and fluid transport in the vadose zone. The distribution of water within rock is important due to its significant influence on rock mechanical behavior. Here, therefore, we used nuclear magnetic resonance (NMR) technology to visualize and quantify the dynamics of water infiltration and distribution in initially unsaturated sandstone. The progression of water imbibition in sandstone specimens under the following two conditions were analyzed: (1) specimens soaked in water for different durations and (2) specimens soaked in water for the same duration and then held in this state for different durations. An analytic function was developed to estimate the sandstone moisture profile and to determine the unsaturated flow within the sandstone when the water distribution matched laboratory observations. Finally, a three-dimensional discrete element grain-based model was formulated that incorporates the local parallel-plate method, the unsaturated flow function, and the generalized effective stress principle. We used this model to effectively reproduce the process of water imbibition in the laboratory sandstone specimens. The effect of water imbibition on the mechanical properties of the studied sandstone was also evaluated. These results show that the strength of the core of the sample was reduced as water migrated from its surface to its center, resulting in a decrease in bulk sample strength as standing duration (i.e. water distribution

uniformity) increased. The results of this study aid in our understanding of the influence of water imbibition on the mechanical behavior of sandstone, which is important for rock slope stability assessments following rainfall.

**Keywords**: nuclear magnetic resonance; unsaturated flow; Voronoi polyhedral; capillary suction; mesoscale

**Highlights**:

- Nuclear magnetic resonance used to monitor water imbibition in sandstone.
- Linear relationship found between wetting front migration and square root of time.
- Strength and Young's modulus decrease as a function of increasing water saturation.
- 3D numerical DEM simulations (3DEC-GBM) are in agreement with experimental data.
- Water saturation is an important consideration in slope stability assessments.

## 1. Introduction

Although water, or aqueous solutions, are ubiquitous in the upper crust, not all of the void space within crustal rocks will be fully saturated. Water imbibition in rocks can occur spontaneously, and is driven by capillary forces and gravity (Richards 1931). The water content in and transport through rock materials are important topics because rocks are weaker when saturated with water (Baud et al. 2000; Brantut et al. 2013). Prediction of the distribution and time-dependence of water content in initially unsaturated rocks is therefore essential to understand the long-term stability of various geotechnical structures, such as rock slopes (Godt et al. 2009; Lu and Godt 2008; Oh and Lu 2015; Yang et al. 2017), underground tunnels (Or et al. 2005), nuclear waste storage facilities (Ghezzehei et al. 2004; Tsang et al. 2015), and petroleum engineering projects (Haugen et al. 2014; Karpyn et al. 2009).

Many studies have been carried out to investigate the strength and deformation characteristics of rocks with different water saturations (Demarco et al. 2007; Heap et al. 2019; Liu et al. 2020; Shakoor and Barefield 2009; Silva et al. 2008; Tang et al. 2018; Vásárhelyi and Ván 2006; Wong et al. 2016; Zhou et al. 2016). Hawkins and McConnell (1992) summarized the influence of water content on the mechanical behavior of 35 different sandstones and found that the reduction in unconfined compressive strength (UCS) from dry to saturated conditions varied from 8.2% in quartz-rich sandstones to up to 78.1% in clayey sandstones. Vásárhelyi (2003) analyzed these data and found a linear correlation between dry and fully saturated UCS. The data compilation provided in Heap et al. (2019) highlights that water-weakening in sandstone increases as a function of increasing clay content. Erguler and Ulusay (2009) presented a quantification of the effects of water content on rock mechanical properties, and developed a method for estimating the strength and deformation properties at any

water content based on their physical properties. However, the analysis presented in Erguler and Ulusay (2009) is based on qualitative descriptions rather than quantitative expressions. Many studies that investigate the influence of water on rock mechanical properties compare the properties of dry and fully saturated samples. Comparatively few experimental studies have been performed on partially saturated samples. For example, Tang et al. (2018) showed that the minimum creep strain rate and time-to-failure in brittle creep experiments on sandstone increased and decreased, respectively, as water pre-immersion duration increased. Most studies, however, do not study how the spatial distribution of water within the sample influences rock mechanical properties. For instance, it is not yet known whether the mechanical properties of two rock specimens that have been soaked in water for the same duration but left to stand for different durations are the same. The mechanical properties of a partially saturated rock are expected to depend on the spatial distribution of the water content at the mesoscale. A small change in water saturation might lead to significant changes in the mechanical properties of rock. Therefore, more information about the influence of water distribution on the mechanical properties of rocks should be obtained.

Non-destructive testing techniques offer the capability to directly measure the distribution of water saturation and to visualize the dynamics of water transport in initially unsaturated rocks. These techniques can be grouped into three classes. (1) X-ray tomography is a noninvasive measurement technique that can be effectively used to visualize and measure moisture transport processes in porous materials (Heindel 2011; Nakashima 2000; Roels and Carmeliet 2006). Akin et al. (2000) studied spontaneous water imbibition into Berea sandstone and diatomite samples using X-ray computerized tomography (CT) and analyzed the influence of pore structure on spontaneous imbibition characteristics. Taud et al. (2005) developed a method to determine the porosity of rock from X-ray CT images without using image segmentation techniques. David et al. (2011) and Pons et al. (2011) studied the influence of damage and strain localization on capillary imbibition and found, for example, that compaction bands slow capillary imbibition in sandstone. David et al. (2017) found that the P-wave velocity of the zone ahead of the imbibition front was higher than that of the unsaturated rock due to moisture effects. Oesch et al. (2019) demonstrated that X-ray computed tomography can be used to measure moisture front movement and distribution over time in concrete. However, X-ray tomography relies on the use of a contrast agent to detect water movement and content distribution in variably-saturated porous media, and the contrast agent may alter the wetting behavior of the porous media. (2) Neutron transmission radiography (NTR) is based on the attenuation (strongly attenuated by hydrogen in water but much less attenuated by gas phases in porous materials) of a neutron beam as it passes through a sample. As a result, NTR has been commonly applied to capture the variations of moisture content during water imbibition in porous materials (El Abd et al. 2013; Perfect et al. 2014; Zhang et al. 2011). Kim et al.

(2011) explored the use of neutron imaging for studying water distribution variation in partially saturated granular materials and investigated the effect of particle morphology on water distribution in compacted granular columns. Zhao et al. (2019) and Zhao et al. (2018) observed temporal changes in the spatial distribution of water in low-permeability sandstones using neutron radiography and demonstrated the sensitivity of sorptivity expressly to the tortuosity rather than porosity of the samples. While NTR is an effective method to investigate hydrogen-rich fluids in porous materials, it requires quite sophisticated and expensive laboratory equipment and specific safety measures. (3) Nuclear magnetic resonance (NMR), which is a well-known technique in medical diagnosis and material science, has been gradually exploited to provide useful information about the various aspects of mass transport in porous materials over the last three decades (Gummerson et al. 1979; Koptyug 2012; Mitchell et al. 2013). Because the NMR technique is tuned to excite the hydrogen nucleus, the technique is particularly sensitive to water molecules. Carpenter et al. (1993) demonstrated that magnetic resonance imaging is a suitable method to measure water content distributions in limestone, and the water content distributions in NMR images are consistent with the predictions of unsaturated flow theory. Meanwhile, care is needed whenever polymer based or organic materials are present, as their hydrogen content may influence results. In the case of cement-based materials, for example, the unknown amount of hydration products compromises the results.

Due to the aforementioned importance of understanding the dynamics of water movement in partially saturated rocks and the significant effect of water content on the mechanical properties of rocks, we first performed non-destructive measurements of the spontaneous imbibition of water into sandstone samples using NMR imaging. The evolution of water imbibition and the distribution of water within the sandstone were visualized using this technique. Then, a three-dimensional discrete element grain-based model (3DEC-GBM) that accounts for the water imbibition process was developed to help quantify water imbibition in the sandstone specimens. Finally, uniaxial compression simulations and direct tensile simulations were carried out on numerical sandstone specimens with different water distributions to understand the influence of the spatial distribution of water on their mechanical behavior.

## 2. Theory for unsaturated flow

It is the tendency of water to imbibe spontaneously into the void space of unsaturated porous media that drives capillary absorption (Bažant and Najjar 1971; Hall and Hoff 2011). An extended Darcy's law, which provide a quantitative basis for modeling the movement of water in rocks (Carpenter et al. 1993; Gummerson et al. 1979) , is usually used to predict the distribution of water content in rocks and its variation with time in response

to diffusion, evaporation, rainwater, and groundwater absorption. It is often a complex non-linear function of the water content and can be given by (Carpenter et al. 1993):

$$u=-K(\theta)F \tag{1}$$

where $u$ is the flow velocity, $K$ is the hydraulic conductivity function, $\theta$ is the ratio of liquid volume to bulk volume (volume fraction saturation), and $F$ is the capillary force.

Combining Eq. 1 with the continuity equation, the governing equation (i.e. Richards equation) of the one-dimensional capillary-driven flow in unsaturated rock is given by (Gummerson et al. 1979; Philip 1960):

$$\frac{\partial\theta}{\partial t}=\frac{\partial}{\partial x}\left(D(\theta)\frac{\partial\theta}{\partial x}\right) \tag{2}$$

where $D(\theta)=K(\theta)(d\Psi/d\theta)$, $D(\theta)$ is the unsaturated hydraulic diffusivity, with dimensions $L^2T^{-1}$. $\Psi$ is the capillary potential. It should be noted that the D(θ) term only describes the water movement due to capillary forces in this case. The influence of gravity is generally assumed to be negligible in Eq. 2.

By introducing the Boltzmann transformation, $\lambda = x/t^{1/2}$, Eq. 2 becomes:

$$-\frac{\lambda}{2}\left(\frac{d\theta}{d\lambda}\right)=\frac{d}{d\lambda}\left(D(\theta)\frac{d\theta}{d\lambda}\right) \tag{3}$$

Subject to the following initial and boundary conditions:

$$\begin{cases}\theta=\theta_i & \lambda\to\infty\\ \theta=\theta_0 & \lambda=0\end{cases} \tag{4}$$

where $\theta_i$ is the initial water content and $\theta_0$ is the specimen boundary water content.

The integration of Eq. 3 between the limits $\theta_i$ and $\theta$ yields:

$$D(\theta)=-\frac{1}{2}\frac{d\lambda}{d\theta}\int_{\theta_i}^{\theta}\lambda d\theta \tag{5}$$

Several approaches that circumvent the difficulties involved in determining the slopes of water distribution curves from experimental data have been proposed (Bažant and Najjar 1972; Philip 1960; Wu and Pan 2003). According to Evangelides et al. (2018); Evangelides et al. (2010), a fitting function with three constants (a, b, and c) for the transformed rock moisture profile can be used of the form:

$$\theta(\lambda)=-\left[\theta_0+a\tan^{-1}(b\lambda+c)\right] \tag{6}$$

The unsaturated hydraulic diffusivity (Eq. 5) as a function of θ using Eq. (6) then becomes:

$$D(\theta)=-0.5\frac{1+\left(\tan\left(-\frac{\theta+\theta_0}{a}\right)\right)^2}{ab}\left(\frac{c}{b}(\theta-\theta_i)+\frac{a}{b}\ln\left(\frac{\left|\cos\left(\frac{\theta_i+\theta_0}{a}\right)\right|}{\left|\cos\left(\frac{\theta+\theta_0}{a}\right)\right|}\right)\right) \tag{7}$$

## 3. Materials and methods

The studied sandstone was collected in Yunnan (China). The mineralogical composition of this sandstone is approximately 60% quartz, 19% feldspar, 8% calcite, and 13% cement (i.e. clay minerals). The grain size of Yunnan sandstone is approximately 100-200 μm. The average dry density of Yunnan sandstone is 2,119 kg/m$^3$, and the connected porosity, calculated using mercury intrusion porosimetry, is 14.2 %. A number of cylindrical specimens were prepared from a single block, with a diameter of 50 mm and a height of 100 mm. No macroscale defects, such as fractures, were observed in any of the prepared specimens.

### 3.1 Nuclear magnetic resonance imaging (NMR)

NMR imaging is a powerful technique that allows determination of the distribution of water content in porous materials and its variation with time in response to evaporation, condensation, rainwater, and groundwater absorption (Carpenter et al. 1993; Mitchell et al. 2013; Zhou et al. 2016). Here, we imaged water imbibition in sandstone specimens using the NMR technique at the School of Sino-Dutch Biomedical and Information Engineering at Northeastern University in Shenyang, China. An Expotus 0.35T instrument was employed to provide the NMR images. The 0.35 T permanent magnet vertical field MRI (Magnetic Resonance Imaging) image can be comparable to the superconducting 0.5T axial field image. This device uses four receiving channel spectrometers and a phased array multichannel coil. The radio-frequency power amplifier is 6 kW and provides a 3 kHz broadband and 180° radio-frequency pulse. All images were stored and transmitted in Dicom (Digital imaging and communications in medicine) format to guarantee the extension and visibility of the scan results.

The basic principle of NMR technique deals with the interaction of the radio frequency energy of hydrogen protons ($^1$H) and a strong magnetic field. The detailed operating procedure employed here is as follows (Fig. 1). (1) The wetted specimen is first placed within the NMR instrument. Prior to applying a magnetic field, all of the hydrogen protons in the specimen rotate on their axis, forming randomly oriented magnets (Fig. 1a). (2) A main magnetic field ($B_0$) is then applied around the specimen, after which all of the proton magnets become aligned. Most of the pole axes of the hydrogen protons, which are in a low-energy state, then become aligned with the field $B_0$. The protons in a high-energy state line up directly opposite to the field $B_0$. However, these protons do not simply orientate either with or against the main magnetic field ($B_0$). The process is akin to a spinning top as it falls to the solid surface. The rate of precession can then be determined exactly using the Larmor frequency equation. Fig. 1b shows all of the processing protons related to a common origin on a 3D graph. When all the opposing vectors are canceled, a net magnetization (M) aligned with the main magnetic field $B_0$ can be obtained

(Fig. 1b). (3) An oscillating radio frequency pulse ($B_1$) is then generated in the vicinity of the protons that matches the hydrogen proton precession frequency (Fig. 1c). The protons absorb energy during this stage and flip into the higher energy state. When the absorbed energy is enough to push 50% of the protons into the high-energy state, the net magnetization (M) pointing with the main magnetic field $B_0$ is reduced to zero as the opposing magnetic forces cancel each other out. The radio frequency pushes the protons to synchronize and spin together, which is the "resonance" portion of an NMR scan. A net horizontal magnetization forms, and is called the "transverse magnetization". (4) Finally, the radio frequency pulse ($B_1$) is turned off. The net magnetization (M) pointing with the main magnetic field $B_0$ gradually generates and energy is released. During this process, a radio signal called the NMR signal is generated and measured by a receiver (Fig. 1d). It is the NMR signal that can describe the spatial information of water molecules and the water imbibition process in initially unsaturated studied sandstones. The NMR imaging employed here detects only hydrogen protons in the unsaturated sandstone sample. The pixel image intensity, derived from spin-echo signal amplitude, is a measure of the spatial distribution of water molecules and therefore provides information on the water imbibition process in the initially unsaturated sandstone.

Fig. 1

### 3.2 Direct measurement of water imbibition

Prior to the imbibition experiments, all specimens were stored in a temperature- (21±2 ℃) and relative humidity- (17±2%) controlled room. Specimens were selected for the imbibition experiments based on their similar porosities, and their initial saturation was close to 5% prior to imbibition. The upper and lower end surfaces of the specimens were made waterproof by coating them with a very thin layer of silicone hydrophobic agent (a liquid) in order to ensure that water absorption occurred exclusively radially through their circumferential surfaces. Table 1 shows the increase in the mass of three samples of the studied sandstone over time (up to 20 mins) during the water absorption process. These three samples were immersed in water and their mass was measured at time intervals of 1 min from the start of the water imbibition process. It can be seen that the rate of water absorption in each sample was high during the initial stage (< 6 mins), after which the rate of water absorption decreased as a function of increasing time (Table 1).

Table 1

The specimens were soaked in a tank filled with distilled water for fixed durations of 30, 90, 180, 300, 480, 720, and 1200 s, after which they were taken out of the water, wiped to remove the free water on their surfaces,

weighed, and coated with a waterproofing membrane (to prevent desaturation). These soaking durations were selected based on the results of our three preliminary imbibition experiments (Table 1). The specimens were then promptly placed in the NMR to obtain images that showed the distribution of water in the sandstone directly. The image acquisition time was set at 120 s in this study, which is relatively rapid compared with the rate of water imbibition. A strategy for identifying the wetting front across the cross-section of the sample is shown in Fig 2a. The water content was taken as the total amount of water in all of the cross-sectional slices along the axis of the cylindrical specimen. Here, the image intensity of a saturated sample was used to provide a convenient calibration, and the gray value extracted from the NMR image of the saturated sample was set to correspond to the volumetric water content of the saturated sample. Moreover, six radial lines in the sample were used to monitor the change in saturation with time. The volumetric water content profiles along these six radial lines following a soaking duration of 180 s (the green line in Fig 2a) are plotted in Fig 2b. The water distribution curves for the six radial lines are approximately equal, which demonstrates that water imbibition in each part of the sample was relatively uniform. Water imbibition along the #1 monitoring line (the green line in Fig 2a) was used in the analysis below. Fig. 3 shows an NMR image of a sandstone specimen after a soaking duration of 180 s, processed using MATLAB®. Specifically, we use our own MATLAB® code to first import the NMR image and then replace each gray value pixel with a blue point to clearly mark the water distribution boundary. The processed NMR image clearly reveals the water distribution in the rock specimens directly (the blue points represent individual water molecules within the specimen).

Fig. 2

Fig. 3

Fig. 4 shows a sequence of water distribution profiles obtained following soaking durations of 30, 90, 180, 300, 480, 720, and 1200 s. We note that the water distribution profiles were very similar along the axis of each sample (i.e. the imbibition process was uniform along the length of the sample in each experiment). As for Fig. 3, the blue points in Fig. 4 represent individual water molecules within the specimen. Due to the low number of water molecules, it is unfortunately not possible to accurately image the distribution of water within the natural sample prior to imbibition using the NMR technique. As water is imbibed into capillaries of a porous medium, the air will be displaced by the advancing wetting front and expelled from the sample (small bubbles of air were continually expelled from the circumferential surface of the sample during the imbibition process). Fig. 4 shows that water molecules migrated from the outer circumferential surface of the cylindrical specimen to its center. For short soaking durations, only a circumferential annulus of the specimen contains water molecules and the center

of the cylinder remained dry. As soaking time increases, water gradually fills the pores within the rock, increasing the water content until the sample approaches complete saturation (complete saturation is rarely obtained during the imbibition process as pores connected to the porosity backbone by narrow pore throats often remain unsaturated, see below). Thus, the distribution of water in the rock is not uniform during the imbibition process. The results clearly demonstrate the effectiveness of NMR in providing high quality, quantitative data for understanding the imbibition process in porous materials such as sandstone.

Fig. 4

Fig. 5a shows the results of water content distribution profile along the #1 monitoring line in samples soaked for different durations. From these profiles, the position of the wetting front was determined, defined as the distance at which the volumetric water content in the circumferential surface of sample is equal to the initial water content of 0.006 $cm^3/cm^3$ (the point where a given time profile intercepts the dotted line shown in Fig. 5a). Water gradually imbibed into the specimen from its circumferential surface to its core during soaking. The speed of imbibition was relatively quick and water reached the core of the sample after about 540 s. The initial water content ($\theta_i$) was 0.006 $cm^3/cm^3$, and final water content ($\theta_0$) reached 0.127 $cm^3/cm^3$. The water gradually filled the pores within the specimen, increasing the water content until the specimen was saturated (Fig. 5a). As water was absorbed by capillary forces in an initially dry porous medium, most of the air was displaced ahead of the advancing wetting front and expelled. However, we note that some air is likely trapped inside the specimen due to disconnected or small isolated pores. Indeed, the connected porosity determined from our mercury injection experiments (14.2%) is higher than the porosity occupied by water following complete imbibition (about 13%).

Fig. 5b shows the volumetric water contents as a function of the Boltzmann variable ($\lambda$) for the sandstone samples. All the water distribution profiles generally converge onto a master line. The deviation of the data for the sandstone soaked for 30 s is likely due to experimental error. The result illustrates that the linearity of the wetting front location as a function of the square root of time, and the profiles maintain a constant shape (Fig. 5c). We assume that the profile can be described by Eq. 6 with three constants under determination, which has previously been shown to be very effective in describing moisture profiles of this form (Evangelides et al. 2018; Evangelides et al. 2010). The theoretical curve (red solid line in Fig. 5b) was obtained and the constants $\theta_0$, a, b, and c were found to be 0.127, 0.19, 3.02 $m^{-1}s^{0.5}$, and -4.40, respectively.

The unsaturated flow function as a function of water content ($\theta$) is presented in Fig. 5d. The unsaturated hydraulic diffusivity ($D(\theta)$) is calculated using Eq. 7 from the calculated constants a, b, and c. We find that the diffusivity of the specimen increases nonlinearly and by several orders of magnitude (i.e. from $10^{-5}$ to $10^{-2}$ $mm^2/s$)

with increasing water content from 0.006 to 0.015 $cm^3/cm^3$. The increased rate of the unsaturated hydraulic diffusivity remained constant above a water content of 0.025 $cm^3/cm^3$ (Fig. 5d).

Fig. 5

Fig. 6 shows θ(t) profiles generated by recording the relationship between the volumetric water content and the elapsed time at different positions (2, 5, 8, 11, 14, 17, 20, and 23 mm) along the radial line #1 in the specimen. The results were consistent with Eq. 6 by fixing the distance (value of x) with the three constants under determination.

Fig. 6

Fig. 7 shows the evolution of water content at different positions in two dimensions inside the specimens following a soaking time of 180 s followed by different standing durations of 120, 240, 480, 720, 960, 1200, 1440, and 1680 s. When the specimen was soaked for 180 s, water only imbibed around the outer surface of the specimen, producing a wet annulus. During standing, water gradually imbibed into the rock from the surface to the center of the sample until the water was evenly distributed within the sample (Fig. 7). Hence, although the specimens contained the same water content, the spatial distribution of water was quite different as a function of increasing standing duration.

Fig. 7

We also present experiments designed to investigate the influence of soaking duration on the water imbibition process in sandstone. Six sandstone specimens were divided into two groups (three specimens per group). (1) For the first group, the specimens were immersed in a tank filled with distilled water for constant durations of 90 s, after which they were taken out of the water, weighed, and coated with the waterproofing membrane (to prevent desaturation). These specimens were then stored for 15 h in a room with a constant temperature (21±2 °C) and humidity (17±2%) to ensure a uniform distribution of water (NMR measurements showed that the distribution of water was uniform in three samples stored for 12, 15, and 18 h). Finally, these specimens again were immersed in a tank filled with distilled water for 30, 90, and 180 s, respectively. (2) For the second group, the specimens were immersed in a tank filled with distilled water for constant durations of 120, 180, and 270 s, respectively. NMR measurements were performed on both groups of samples. Fig 8 shows the distribution of water content for the two groups of specimens. The water content of the sample soaked twice was much higher than that of the sample soaked once for the same total duration. For example, the water content of the sample soaked for 180 s in first group was 3.88 %, and the water content of the sample soaked for the same duration in second group was 2.99 %. The wetting front position of the sample soaked twice also was closer to the core of the sample than that

of the sample soaked once for the same total duration. These results suggest that the imbibition of water in the sample is enhanced by allowing the water time to infiltrate the sample for 15 h (not in contact with the water) between soakings.

Fig. 8

### 3.3 Unsaturated flow model

The studied sandstone is composed of interlocking mineral grains and microstructural defects (i.e. pores, grain boundaries, and microcracks). Amongst these microstructural defects, the primary channels for fluid transport are provided by the larger pores (often simply called "pores" or "nodal pores") connected via narrow pore-like channels (usually known as "pore throats"), while the storage volume for fluids such as water is provided by the total available void space (Bakke and Øren 1997; Bernabe 1991; Wardlaw et al. 1987; Zhang et al. 2002) (Fig. 10a). According to the capillary law (Li 2016; Tokunaga and Wan 1997), water bridges are more likely to initially invade and saturate the pores with smaller apertures. In this study, a three-dimensional Voronoi tessellation model (3DEC-GBM), consisting of an assemblage of Voronoi polyhedral grains with variable sizes and shapes, was built using Neper (a software package for polycrystal generation and meshing) (Quey et al. 2011). This model can accurately describe the typical meso-structural features and arrangement of mineral grains of the studied sandstone (Ghazvinian et al. 2014; Li et al. 2017; Müller et al. 2018; Wang and Cai 2018) (see Fig. 9). We incorporated the local parallel-plate model into the 3DEC-GBM model to represent these rough-walled pathways by dividing the contacts into a few parallel-plate sub-regions (i.e. sub-contacts) that were each assigned different apertures (Fig. 10b). The sub-contact aperture distribution used in the 3DEC-GBM was assigned according to the pore diameters distribution of Yunnan sandstone obtained from mercury intrusion porosimetry (Fig. 10c). The pore diameters of Yunnan sandstone followed an approximately lognormal distribution (Fig. 10c). Numerical cylindrical specimens with a diameter of 50 mm and a height of 100 mm (the same dimensions as for the laboratory experiments described in this paper) were generated, and each specimen consisted of 5,300 Voronoi polyhedron grains. Although this number of grains results in an average grain size larger than observed in Yunnan sandstone, creating samples with a small grain size (i.e. samples containing a great number of Voronoi polyhedron grains) is not currently possible due to limitations in computing power. However, Fabjan et al. (2015) showed that the influence of the polygon size on rock strength can be eliminated by having more than ten polygons along the diameter of the specimen's cross-section and 5,300 polygons agrees well with the discretization of the numerical samples in other studies, such as Ghazvinian et al. (2014).

The unsaturated flow theory, which governs the imbibition process of the water from the lateral surface to the core of the sandstone specimen, was also introduced into the 3DEC-GBM to mimic the water imbibition process in Yunnan sandstone. In our model, we assumed that the grain boundaries of the sandstone were permeable and provided the primary water transport pathway and storage volume for the imbibed water. Each sub-contact in the model comprises solid-solid contact points and pore space with a constant aperture value (Fig. 10b). For a grain-to-grain contact, according to the capillary law, the water occupies and saturates the sub-contacts with smaller apertures, and all sub-contacts with larger apertures contain air and water vapor. The saturation degree of the contact is given by Eq. (8):

$$S_e = \frac{\sum_{i}^{m} b_i A_i}{\sum_{i}^{n} b_i A_i} \quad (8)$$

where $b_i$ is aperture of the *ith* sub-contact of the contact, $A_i$ is area of the sub-contact of the contact, $n$ is the total number of sub-contacts of the contact, and $m$ is the number of sub-contacts with smaller apertures occupied by water of the contact. In our model, the aperture of the sub-contacts is assumed to be 1-60 μm.

Fig. 9

Fig. 10

The sequential images of the evolution of water imbibition with time are shown in Fig. 11. The position of the wetting front was also determined as a function of time. As soaking duration increased (more water imbibes into the specimen), the wetting front reached the core of the sample, and then the water content at the core of the sample continued to increase until it reached full saturation. The modeled imbibition of water is very similar to that observed during the experiments. Based on the experimental results shown in Fig. 5, we performed numerical simulations to show the sequence of time-lapse spatial water content in the studied sandstone with a constant water content corresponding to a saturation degree of 49.3% (soaking time 180 s) (Fig. 12). Fig. 12 shows the water initially remained only near the surface of the sample, producing a wet outer annulus. Then, the water gradually migrated from the surface to the core of specimen until the water distribution was uniform.

Fig. 11

Fig. 12

## 4. Effect of water distribution on the mechanical properties of sandstone

During capillary imbibition, the distribution of water within the rock specimens was not uniform: the rock

specimens were saturated around an outer annulus but dry in their cores. Whether the non-uniform distribution of water in sandstone has an influence on the mechanical properties of sandstone is an important question to address and will be the focus of this section.

### 4.1 Generalized effective stress induced by capillary phenomena

The capillary effect occurs whenever the pore space is partially-saturated with at least two immiscible fluids, such as gas and water (Eeckhout 1976; Schmitt et al. 1994; Tokunaga and Wan 1997; West 1994; Zeng et al. 2013). Capillary pressure is created by liquid menisci in the pores between mineral grains. It has been demonstrated that the weakening of rocks (e.g., shale, chalk, sandstone, mudstone, and gypsum) can be attributed to a decrease in capillary tension. The capillary pressure is then given by Eq. (9), which describes the relationship between capillary pressure and saturation (Itasca 2018). Eq. (9) has the same form as the van Genuchten curve (Van Genuchten 1980), but it takes into account the effect of microcrack aperture.

$$P_c\left(S_e,\mathrm{b}\right)=p_a-p_w=\alpha\rho_w g\frac{b_0}{b}\left(S_e^{\frac{\beta}{1-\beta}}-1\right)^{1/\beta} \tag{9}$$

where $P_c$ is capillary pressure, $S_e$ is the saturation degree, $p_a$ is pressure in air or the non-wetting phase, $p_w$ is pressure in water or the wetting phase, $b_0$ is the relative specific opening degree corresponding to the microcrack saturation, $b$ is the local microcrack aperture, $g$ is the acceleration due to gravity, $\rho_w$ is the density of water, and $\alpha$ and $\beta$ are constants related to capillary pressure curves.

To explain the influence of water on the mechanical behavior of partially saturated rock, Rozhko (2011) and Schmitt et al. (1994) introduced a generalized effective stress relation, established on rocks partially-saturated with air and water:

$$\sigma'=\sigma-p_a+\delta\left(p_a-p_w\right) \tag{10}$$

where, $\sigma'$ is the total stress, and $\delta$ is the additive coefficient and is equal to saturation degree $S_e$. We further assumed that the total air pressure is equal to atmosphere pressure, $p_a$=*101.325 kPa*.

The formulation of a generalized effective stress can be obtained from Eqs. (9) and (10) as follows:

$$\sigma'=\sigma+\alpha\rho_w g\frac{S_e b_0}{b}\left(S_e^{\frac{\beta}{1-\beta}}-1\right)^{1/\beta}-p_a \tag{11}$$

The generalized effective stress theory was introduced into the 3DEC-GBM to conduct uniaxial compression simulations of the partially saturated sandstone. The implementation of the generalized effective stress theory in the 3DEC-GBM is based on the following four assumptions. (1) The grains are assigned to be linear elastic without

372 an ultimate strength and the contacts between grains follow two contact criteria: Rankine's maximum tensile stress
373 criterion and the Mohr-Coulomb shear failure criterion (Ghazvinian et al. 2014). (2) Both tensile and shear failure
374 criteria of the rock are expressed in terms of the generalized effective stress, not total stress. (3) Water bridges are
375 more likely to initially invade and saturate the pores in the sandstone with narrow apertures (Tokunaga and Wan
376 1997) (see Fig. 3a). (4) The capillary phenomenon only occurs at sub-contacts between grains and does not affect
377 the grains themselves. The capillary pressure affects the sub-contact normal deformation.

378 **4.2 Sensitivity of strength and deformability characteristics to changes in water distribution in the**
379 **sandstone**

380 Sandstone specimens were first soaked in water for different durations to prepare specimens with different
381 water contents (0.8, 1.48, 2.76, and 6.1%). They were subsequently removed from the water, weighed, and coated
382 with paraffin wax and a waterproofing membrane (to prevent desaturation). The samples were then kept for 24 h
383 to ensure that the water was evenly distributed in the sample. Finally, the specimens were subjected to uniaxial
384 compression strength (UCS) testing applied a constant displacement rate of 0.0025 mm/s. The results of the
385 uniaxial compression experiments on Yunnan sandstone containing different levels of water saturation are shown
386 in Fig 13. These results are consistent with previous experimental studies that have also shown that saturation
387 with water decreases the strength and Young's modulus of sandstone (see Baud *et al.*, 2000; Heap *et al.*, 2019;
388 Tang et al., 2018).

389 Based on the above experimental results, we used a similar calibration method to that presented in
390 Ghazvinian et al. (2014) to calibrate the mesoscale mechanical parameters of the partially saturated model with a
391 uniform water distribution. A series of numerical simulations using the generalized effective stress law were first
392 conducted to determine the appropriate capillary pressure curve parameters. The calibrated capillary parameter
393 was found to be $\beta = 1.51$. The calibrated meso-mechanical parameters for saturated sandstone are listed in Table
394 2. Fig. 13 shows that the strengths of the modeled samples with water saturation of 13.1, 24.3, 45.2, and 100%
395 were 52.3, 48.5, 42.2, and 38.3 MPa, respectively. We find that the numerical simulations accurately reproduce
396 the mechanical behavior (e.g., the elastic modulus) and strength of the laboratory experiments (Fig. 13)

397 Table 2

398 Fig. 13

399 Combining the above model with the generalized effective stress law, we can study the influence of non-
400 uniform water distribution on the mechanical properties of Yunnan sandstone. We deformed numerical samples
401 that have the same water content (a saturation degree of 49.3%) but different standing durations (Fig. 14 and 15).

The axial stress was determined by calculating the sum of the z-direction forces on the top surface divided by the cross-sectional area of the sample (i.e. the same method used for the laboratory experiment) in Fig. 14. It can be seen from Fig. 14 that the UCS and the uniaxial direct tensile strength (UTS) decreased linearly as the water distribution became increasingly uniform in the specimen. For example, the compressive strength was reduced from 42.1 to 41.0 MPa, as the standing time was increased from 120 s to 1680 s, a reduction close to 2.68 % (Fig. 14). Similarly, the Young's modulus determined from these simulations also exhibits a water-distribution dependency. The Young's modulus of simulated sandstone increased from 8.82 to 10.33 GPa as the standing time (i.e. water distribution uniformity) was increased from 120 to 1680 s. These results show that the distribution of water within samples characterized by the same water content resulted in small decreases to the UCS and UTS and small increases to the Young's modulus of sandstone (Fig. 14).

We also studied the influence of water distribution on the mechanical properties of zones within the sandstone specimens. The axial stress was calculated here by monitoring the average zone stress $\sigma_{zz}$ for all blocks in the central region of the model (Fig. 15). Fig. 15a shows the stress-strain curves (axial stress is measured in the central 20 mm × 20 mm × 40 mm zone) for specimens with constant water content (saturation degree 49.3%), but different standing durations. The simulation results indicate that the strength (peak stress) of the central part of the samples decreased with increasing standing duration (i.e. as the water migrated from the surface of the sample to its interior). Fig. 15b shows the stress-strain curves (axial stress is measured in the different central zones) for specimens with a constant water content (saturation degree 49.3%) and standing duration (120 s). The results indicate that the strength (peak stress) decreased as the measured region of axial stress within a cube in the center of the specimen increased. The results of these simulations demonstrate that the distribution of strength within the sample is nonuniform as a direct result of the nonuniform distribution of water.

Fig. 14

Fig. 15

## 5. Discussion

The results from the capillary imbibition processes presented in this study illustrate that the distance of the wetting front from the outer circumferential surface of the sample increases linearly with the square root of time, in agreement with previous studies by David et al. (2011) and Zhao et al. (2017)). However, the rates of water imbibition in the Bentheim sandstone (Germany; porosity = 24.4%) studied by David et al. (2011) and in the silty (i.e. clay rich) sandstone (also from Yunnan Province; porosity = 15.2%) studied by Zhao et al. (2017)) were faster

and slower than that of Yunnan sandstone (porosity = 12.93%), respectively. Based on the porosity alone, it is perhaps surprising that the rate of imbibition is higher in Yunnan sandstone than in the silty sandstone studied by Zhao et al. (2017)); however, these data highlight the important role of pore size in the imbibition process. The majority of pores in Bentheim sandstone, Yunnan sandstone, and the silty sandstone from Yunnan Province are 10-50 μm, 5-10 μm, and 1-5 μm, respectively. Moreover, the presence of clay minerals also has an important influence on the rate of water imbibition. David et al. (2011) illustrated, using X-ray imaging during imbibition experiments on Vosges sandstone (France) and Bentheim sandstone, that clay minerals coating or filling pores significantly modified the capillary process in these porous rocks. Zhao et al. (2017)) indicated that the interaction between clay minerals and water could lead to more complex pore structures including a large tortuosity and small capillary size, and a high sensitivity of sorptivity to tortuosity rather than porosity. Therefore, the lower rate of imbibition in the silty sandstone compared with Yunnan sandstone is likely a combination of its smaller pore size and higher clay content.

The uniaxial compressive strength is significantly reduced for Yunnan sandstone as saturation is increased from 0 to 40%, which is consistent with the results described in Shakoor and Barefield (2009). Shakoor and Barefield (2009) proposed empirical equations to estimate the uniaxial compressive strength of sandstone as a function of increasing water saturation for four absorption classes. According to the empirical predictive equation for sandstone with absorption class D (absorption = 6 ~ 7%) proposed by Shakoor and Barefield (2009), the uniaxial compressive strength of fully saturated Yunnan sandstone (absorption = 6.1%) is estimated to be 42.4 MPa. However, the uniaxial compressive strength of fully saturated Yunnan sandstone was measured to be 38.3 MPa, lower than the uniaxial compressive strength predicted using the method of Shakoor and Barefield (2009) (Fig. 16a). Fig. 16a shows that the modeled strength as a function of increasing water saturation is different from that of the measured strength. Different clay minerals content in these sandstones may account for this discrepancy. Hawkins and McConnell (1992) suggested that the strength of sandstones containing abundant clay minerals is significantly reduced upon wetting, which is likely to be related to the softening and possible expansion of the clay minerals. For example, Millstone Grit (Type A) sandstone and Millstone Grit (Type D) sandstone studied in Hawkins and McConnell (1992) and Yunnan sandstone contain 13.9%, 9.2%, and 13% clay minerals, respectively. The difference between $UCS_{dry}$ and $UCS_{sat}$ for Millstone Grit (Type A) sandstone, Millstone Grit (Type D), and Yunnan sandstone were about 33.2, 22.7, and 32%, respectively. The empirical predictive equation of Shakoor and Barefield (2009) is based upon data collected from Berea B sandstone and Cow Run sandstone, the clay contents of which are 3.6 and 2.6%, respectively. Therefore, the difference between our data and the modeled

uniaxial compressive strength (Fig. 16a) is likely due to the high clay content of the studied sandstone. Nevertheless, the empirical model of Shakoor and Barefield (2009) provides a reasonable estimate of the strength of Yunnan sandstone as a function of increasing water content (Fig. 16a). Fig. 16b shows a graph of relative UCS as a function of water saturation for the sandstones studied in Demarco et al. (2007) and for Yunnan sandstone (the data of this study). These data show that the uniaxial compressive strength of sandstones decreases as a function of increasing water saturation and that the data from Demarco et al. (2007) are consistent with the new data for Yunnan sandstone (Fig. 16b). The data from Demarco et al. (2007) highlight that the strength of sandstones containing more accessory minerals (i.e. less quartz) and expanding clays is reduced more upon saturation than pure (i.e. quartz-rich) sandstones. For example, the strength of Bad Bentheim sandstone (quartz content = 98%) was only reduced by about 5% upon complete saturation, whilst the strength of Schleeriether sandstone (quartz content = 80%), a sandstone that also contains expanding clays, was reduced by about 60% (Demarco et al. 2007). As discussed above, we consider the strength reduction upon saturation in Yunnan sandstone (a reduction of about 33%; Fig. 16b) as the result of the presence of clays (see also Heap et al. 2019).

Fig. 16

Our simulations showed that increasing the standing time (i.e. increasing the uniformity of water distribution) resulted in a decrease in uniaxial compressive strength (Fig. 15a). When the water is confined to the outer edge of the sample (i.e. for short standing durations), the presence of a dry sample core, which is stronger due to the weakening influence of water (see Fig. 16), results in a higher bulk sample strength. As the water migrates towards the sample core (i.e. as the standing duration and water distribution uniformity increases), the volume of the dry sample core is reduced (Fig. 12) and therefore the bulk sample strength is reduced. Water distribution, for a given volume of water, can influence bulk sample strength because water-weakening in sandstones does not require 100% water saturation (see Fig. 16). These results demonstrate that both the water content (saturation) and the water distribution (uniformity) exert first-order controls on the mechanical behavior of sandstone.

The main underlying mechanisms that promote the observed reduction in rock strength in the presence of water include a reduction of fracture energy, capillary tension, and friction, an increase in pore fluid pressure, and chemical and corrosive deterioration. Water-weakening processes can be grouped as either mechanical or chemical mechanisms. Mechanically, stress is partitioned between the rock matrix and the pore fluid. Pressurized pore fluids act to reduce the applied normal stresses and thus tend to reduce the strength of rocks. A marked decrease in strength is also observed with an increase in moisture content in rocks. Chemically, rock-fluid interaction occurs through stress corrosion reactions (e.g., (Brantut et al. 2013; Heap et al. 2009) or a reduction in

fracture energy. None of these mechanisms can be discounted outright, but some are more important than others for certain rock types and certain loading conditions. In this study, capillary effects were used to explain the observed water-weakening in Yunnan sandstone. It was shown that wet sandstone weakening can be attributed to a release of capillary suction between grains, which is linked to pore size distribution. Papamichos et al. (1997), Schmitt et al. (1994), and West (1994) also experimentally showed that the capillary forces can cause a major change in the strength in various rocks (such as shale, chalk, limestone, and sandstone). In addition, Baud et al. (2000) concluded that water-weakening in sandstone was the result of reductions to both the specific surface energy and the friction coefficient. Arsalan et al. (2013) quantified the relationship between the surface energy characterization of sandstone and fluids using IGC (Inverse Gas Chromatography), XRD (X-ray diffraction) and XPS (X-ray Photoelectron Spectroscopy) techniques. These authors found that the Lifshitz–van der Waals component of surface energy decreased as a function of increasing water coverage. Atkinson (1984) and Meredith and Atkinson (1983) showed that stress corrosion, a weakening reaction of the bond structure in rock through chemical reaction with the pore fluid, is considered to be one of the key factors driving the time-dependent deformation behavior of rocks in the upper crust. Hence, it is necessary to conduct more detailed factor analysis (e.g., mineral component, water content, and temperature) to understand the physicochemical details of water-weakening mechanisms and investigate which water-weakening mechanisms are predominant for a specific rock.

Groundwater or rainwater can be fresh water or saline water with variable electrolyte concentrations. Knowledge of the unsaturated flow of solutes (e.g., $Na^+$, $K^+$, $I^-$ and $Cl^-$) in the pore water of rocks is essential for a quantitative understanding of water-rock interactions in the Earth's upper crust. In this paper, we only studied the imbibition law of distilled water, and did not consider the influence of solutes in the water on water imbibition in initially unsaturated rocks. Further progress therefore requires consideration of the electrolyte concentration and non-neutral values of pH in aqueous fluids to make significant advances in studying the transport of aqueous solutions in the upper crust. It also is necessary to focus future modeling studies on the effects of hydrochemical erosion (e.g., different pH values and chemical compositions of chemical solution) on the deformation characteristics and microstructure of rocks to have a better understanding of the fracturing behavior of rock in real sub-surface environments. For example, Nara et al. (2009) and Nara et al. (2018) performed double torsion experiments using the load relaxation method to investigate subcritical crack growth in rock in distilled water and in an aqueous solution of sodium hydroxide (NaOH, $Ca(OH)_2$) under conditions of controlled temperature, which provide the basis for investigating the influence of electrolyte concentration on time-dependent behavior of rocks. Nara et al. (2018), for example, found that the subcritical crack growth index of granite within an aqueous solution

of sodium hydroxide was higher than that in distilled water. However, Heap et al. (2018) found that the short-term strength of samples of sandstone saturated with geothermal brine and deionized water was essentially equal. Experiments and modeling using different solutions therefore offers an exciting avenue for future research.

The analysis and forecast of the temporal and spatial distribution of water represent meaningful aspects of slope stability assessment since the strength of rock, and therefore the stability of a rock slope, is reduced in the presence of water. Since the penetration and accumulation of water in initially unsaturated rocks can occur following rainfall by capillary forces and gravity, it is important to understand the process of capillary imbibition and its influence on the mechanical behavior and strength of rock to improve assessments of slope stability following rainfall (Collins and Znidarcic 2004; Qi et al. 2003; Tsai and Wang 2011). In this study, we investigated the dynamic process of water imbibition in real time in sandstone specimens and analyze influence of water distribution on the mechanical properties of sandstone at the scale of a laboratory sample (i.e. tens of centimeters). Large-scale experiments and modeling are further required to better understand the imbibition of water into large fractured rock masses with discontinuities such as joints and fractures that can influence fluid flow.

## 6. Conclusions

In this paper, NMR technology was applied as a powerful imaging tool to visualize the dynamic process of water imbibition in real time in sandstone specimens. The water imbibition process from the lateral surface to the core of specimen was quantified as a function of increasing soaking duration. We found a strong linear relationship between the migration of the wetting front and the square root of time, as reported in previous experimental studies (Carpenter et al. 1993; Zhao et al. 2018). The analysis, based on the Richards equation and an empirical function with three constants, yielded relationships between the water content and time and distance. The results show that moisture profiles at specific distances and times could be predicted with acceptable accuracy. The value of unsaturated hydraulic diffusivity increased nonlinearly over several orders of magnitude (i.e. from $10^{-5}$ to $10^{-2}$ $mm^2/s$) as water content increased from 0.006 to 0.015 $cm^3/cm^3$. A three-dimensional discrete element grain-based model (3DEC-GBM), that used the local parallel-plate method and the unsaturated flow function, was generated to simulate the spontaneous imbibition of the water into the sample, which successfully reproduced the water imbibition process observed in the laboratory experiments. The generalized effective stress principle and water unsaturated flow law were further incorporated into the 3DEC-GBM to investigate the influence of water distribution on the mechanical deformation and fracture propagation in the studied sandstone. The simulation results show that the strength of the center of the sample was reduced as water migrated from the surface of the

sample to its core, resulting in a decrease in bulk sample strength as standing duration (i.e. water distribution uniformity) increased. The results of this study are also an important consideration when preparing slope stability assessments following rainfall.

**Acknowledgments**

The work was jointly supported by National Natural Science Foundation of China (51974062, 41672301, 51950410595), National Key Research and Development Program of China (2017YFC1503100), Fundamental Research Funds for the Central Universities of China (N180101028), a Royal Society International Exchange grant, United Kingdom (IEC\NSFC\170625), and a Partenariats Hubert Curien (PHC) Cai Yuanpei grant, France (36605ZB). The comments of two reviewers, and the editor, helped improve this paper.

560 **References**


561 Akin, S., Schembre, J., Bhat, S. & Kovscek, A. 2000. Spontaneous imbibition characteristics of diatomite. Journal of
562 Petroleum Science and Engineering, **25**, 149-165.

563 Arsalan, N., Palayangoda, S., Burnett, D.J., Buiting, J.J. & Nguyen, Q.P. 2013. Surface energy characterization of
564 sandstone rocks. Journal of Physics and Chemistry of Solids, **74**, 1069-1077.

565 Atkinson, B.K. 1984. Subcritical crack growth in geological materials. Journal of Geophysical Research: Solid Earth,
566 **89**, 4077-4114.

567 Bakke, S. & Øren, P.E. 1997. 3-D pore-scale modelling of sandstones and flow simulations in the pore networks. Spe
568 Journal, **2**, 136-149.

569 Baud, P., Zhu, W. & Wong, T.F. 2000. Failure mode and weakening effect of water on sandstone. Journal of Geophysical
570 Research: Solid Earth, **105**, 16371-16389.

571 Bažant, Z. & Najjar, L. 1971. Drying of concrete as a nonlinear diffusion problem. Cement and Concrete Research, **1**,
572 461-473.

573 Bažant, Z. & Najjar, L. 1972. Nonlinear water diffusion in nonsaturated concrete. Matériaux et Construction, **5**, 3-20.

574 Bernabe, Y. 1991. Pore geometry and pressure dependence of the transport properties in sandstones. International
575 Journal of Rock Mechanics & Mining Sciences & Geomechanics Abstracts, **56**, 436.

576 Brantut, N., Heap, M.J., Meredith, P.G. & Baud, P. 2013. Time-dependent cracking and brittle creep in crustal rocks: A
577 review. Journal of Structural Geology, **52**, 17-43, doi: 10.1016/j.jsg.2013.03.007.

578 Carpenter, T., Davies, E., Hall, C., Hall, L., Hoff, W. & Wilson, M. 1993. Capillary water migration in rock: process
579 and material properties examined by NMR imaging. Materials and structures, **26**, 286.

580 Collins, B.D. & Znidarcic, D. 2004. Stability analyses of rainfall induced landslides. Journal of geotechnical and
581 geoenvironmental engineering, **130**, 362-372.

582 David, C., Menendez, B. & Mengus, J.M. 2011. X‐ray imaging of water motion during capillary imbibition: Geometry
583 and kinetics of water front in intact and damaged porous rocks. Journal of Geophysical Research, **116**.

584 David, C., Sarout, J., Dautriat, J., Pimienta, L.X., Michee, M., Desrues, M. & Barnes, C. 2017. Ultrasonic monitoring
585 of spontaneous imbibition experiments: Precursory moisture diffusion effects ahead of water front. Journal of
586 Geophysical Research, **122**, 4948-4962.

587 Demarco, M.M., Jahns, E., Rüdrich, J.r., Oyhantcabal, P. & Siegesmund, S. 2007. The impact of partial water saturation
588 on rock strength: an experimental study on sandstone. Ztschrift Der Deutschen Gesellschaft Für Geowissenschaften,
589 **158**, 869-882.

590 Eeckhout, E.V. 1976. The Mechanisms of Strength Reduction due to Moisture in Coal Mine Shales. International
591 Journal of Rock Mechanics and Mining Sciences & Geomechanics Abstracts, **13**, 61-67.
592 El Abd, A., Abdel-Monem, A. & Kansouh, W. 2013. Experimental determination of moisture distributions in fired clay
593 brick using a 252Cf source: A neutron transmission study. Applied Radiation and Isotopes, **74**, 78-85.
594 Erguler, Z. & Ulusay, R. 2009. Water-induced variations in mechanical properties of clay-bearing rocks. International
595 Journal of Rock Mechanics and Mining Sciences, **46**, 355-370.
596 Evangelides, C., Arampatzis, G., Tsambali, A.-A., Tzanetaki, E. & Tzimopoulos, C. 2018. Moisture estimation in
597 building materials with a simple procedure. Construction and Building Materials, **164**, 830-836.
598 Evangelides, C., Arampatzis, G. & Tzimopoulos, C. 2010. Estimation of soil moisture profile and diffusivity using
599 simple laboratory procedures. Soil science, **175**, 118-127.
600 Ghazvinian, E., Diederichs, M. & Quey, R. 2014. 3D random Voronoi grain-based models for simulation of brittle rock
601 damage and fabric-guided micro-fracturing. Journal of Rock Mechanics and Geotechnical Engineering, **6**, 506-521.
602 Ghezzehei, T., Trautz, R., Finsterle, S., Cook, P. & Ahlers, C. 2004. Modeling coupled evaporation and seepage in
603 ventilated cavities. Vadose Zone Journal, **3**, 806-818.
604 Godt, J.W., Baum, R.L. & Lu, N. 2009. Landsliding in partially saturated materials. Geophysical research letters, **36**.
605 Gummerson, R., Hall, C., Hoff, W., Hawkes, R., Holland, G. & Moore, W. 1979. Unsaturated water flow within porous
606 materials observed by NMR imaging. Nature, **281**, 56.
607 Hall, C. & Hoff, W.D. 2011. Water transport in brick, stone and concrete. CRC Press.
608 Haugen, Å., Fernø, M., Mason, G. & Morrow, N. 2014. Capillary pressure and relative permeability estimated from a
609 single spontaneous imbibition test. Journal of Petroleum Science and Engineering, **115**, 66-77.
610 Hawkins, A. & McConnell, B. 1992. Sensitivity of sandstone strength and deformability to changes in moisture content.
611 Quarterly Journal of Engineering Geology and Hydrogeology, **25**, 115-130.
612 Heap, M.J., Baud, P., Meredith, P.G., Bell, A.F. & Main, I.G. 2009. Time-dependent brittle creep in Darley Dale
613 sandstone. Journal of Geophysical Research, **114**, doi: 10.1029/2008jb006212.
614 Heap, M.J., Reuschlé, T., Kushnir, A.R.L. & Baud, P. 2018. The influence of hydrothermal brine on the short-term
615 strength and elastic modulus of sandstones from exploration well EPS-1 at Soultz-sous-Forêts (France).
616 Geothermal Energy, **6**, 29.
617 Heap, M.J., Villeneuve, M., Kushnir, A.R., Farquharson, J.I., Baud, P. & Reuschlé, T. 2019. Rock mass strength and
618 elastic modulus of the Buntsandstein: an important lithostratigraphic unit for geothermal exploitation in the Upper
619 Rhine Graben. Geothermics, **77**, 236-256.

620 Heindel, T.J. 2011. A review of X-ray flow visualization with applications to multiphase flows. Journal of Fluids
621 Engineering, **133**, 074001.
622 Itasca. 2018. UDEC. *Minneapolis, MN, USA: Itasca Consulting Group Inc.*
623 Karpyn, Z., Halleck, P. & Grader, A. 2009. An experimental study of spontaneous imbibition in fractured sandstone
624 with contrasting sedimentary layers. Journal of Petroleum Science and Engineering, **67**, 48-56.
625 Kim, F.H., Penumadu, D. & Hussey, D.S. 2011. Water distribution variation in partially saturated granular materials
626 using neutron imaging. Journal of geotechnical and geoenvironmental engineering, **138**, 147-154.
627 Koptyug, I.V. 2012. MRI of mass transport in porous media: drying and sorption processes. Progress in nuclear
628 magnetic resonance spectroscopy, **65**, 1.
629 Li, X.F., Li, H.B. & Zhao, Y. 2017. 3D polycrystalline discrete element method (3PDEM) for simulation of crack
630 initiation and propagation in granular rock. Computers and Geotechnics, **90**, 96-112, doi:
631 10.1016/j.compgeo.2017.05.023.
632 Li, Y. 2016. Unsaturated hydraulic properties of rock fractures and their variation law. Rock and Soil Mechanics, **37**,
633 2254-2262.
634 Liu, H., Zhu, W., Yu, Y., Xu, T., Li, R. & Liu, X. 2020. Effect of water imbibition on uniaxial compression strength of
635 sandstone. International Journal of Rock Mechanics and Mining Sciences, **127**, 104200.
636 Lu, N. & Godt, J. 2008. Infinite slope stability under steady unsaturated seepage conditions. Water Resources Research,
637 **44**.
638 Meredith, P.G. & Atkinson, B.K. 1983. Stress corrosion and acoustic emission during tensile crack propagation in Whin
639 Sill dolerite and other basic rocks. Geophysical Journal International, **75**, 1-21.
640 Mitchell, J., Chandrasekera, T., Holland, D., Gladden, L. & Fordham, E. 2013. Magnetic resonance imaging in
641 laboratory petrophysical core analysis. Physics Reports, **526**, 165-225.
642 Müller, C., Frühwirt, T., Haase, D., Schlegel, R. & Konietzky, H. 2018. Modeling deformation and damage of rock salt
643 using the discrete element method. International Journal of Rock Mechanics and Mining Sciences, **103**, 230-241,
644 doi: 10.1016/j.ijrmms.2018.01.022.
645 Nakashima, Y. 2000. The use of X-ray CT to measure diffusion coefficients of heavy ions in water-saturated porous
646 media. Engineering Geology, **56**, 11-17.
647 Nara, Y., Harui, T. & Kashiwaya, K. 2018. Influence of calcium ions on subcritical crack growth in granite. International
648 Journal of Rock Mechanics and Mining Sciences, **102**, 71-77.
649 Nara, Y., Takada, M., Igarashi, T., Hiroyoshi, N. & Kaneko, K. 2009. Subcritical crack growth in rocks in an aqueous

environment. Exploration Geophysics, **40**, 163-171.

Oesch, T., Weise, F., Meinel, D. & Gollwitzer, C. 2019. Quantitative in-situ analysis of water transport in concrete completed using X-ray computed tomography. Transport in porous media, **127**, 371-389.

Oh, S. & Lu, N. 2015. Slope stability analysis under unsaturated conditions: Case studies of rainfall-induced failure of cut slopes. Engineering Geology, **184**, 96-103.

Or, D., Tuller, M. & Fedors, R. 2005. Seepage into drifts and tunnels in unsaturated fractured rock. Water Resources Research, **41**.

Papamichos, E., Brignoli, M. & Santarelli, F.J. 1997. An experimental and theoretical study of a partially saturated collapsible rock. Mechanics of Cohesive-frictional Materials, **2**, 251-278.

Perfect, E., Cheng, C.-L., Kang, M., Bilheux, H., Lamanna, J., Gragg, M. & Wright, D. 2014. Neutron imaging of hydrogen-rich fluids in geomaterials and engineered porous media: A review. Earth-Science Reviews, **129**, 120-135.

Philip, J. 1960. General method of exact solution of the concentration-dependent diffusion equation. Australian Journal of Physics, **13**, 1.

Pons, A., David, C., Fortin, J., Stanchits, S., Menendez, B. & Mengus, J.M. 2011. X-ray imaging of water motion during capillary imbibition: A study on how compaction bands impact fluid flow in Bentheim sandstone. Journal of Geophysical Research, **116**.

Qi, G., Huang, R., Su, B., Hu, Y. & Zhan, M. 2003. Numerical simulation on rainfall infiltration on rock slope. Chinese Journal of Rock Mechanics and Engineering, **22(4)**, 625-629.

Quey, R., Dawson, P.R. & Barbe, F. 2011. Large-scale 3D random polycrystals for the finite element method: Generation, meshing and remeshing. Computer Methods in Applied Mechanics and Engineering, **200**, 1729-1745, doi: 10.1016/j.cma.2011.01.002.

Richards, L.A. 1931. Capillary conduction of liquids through porous mediums. Physics, **1**, 318-333.

Roels, S. & Carmeliet, J. 2006. Analysis of moisture flow in porous materials using microfocus X-ray radiography. International Journal of Heat and Mass Transfer, **49**, 4762-4772.

Rozhko, A.Y. 2011. Capillary phenomena in partially-saturated rocks: theory of effective stress. *45th US Rock Mechanics/Geomechanics Symposium*. American Rock Mechanics Association.

Schmitt, L., Forsans, T. & Santarelli, F. 1994. Shale testing and capillary phenomena. International Journal of Rock Mechanics and Mining Sciences & Geomechanics Abstracts, **31**, 411-427.

Shakoor, A. & Barefield, E.H. 2009. Relationship between unconfined compressive strength and degree of saturation

for selected sandstones. Environmental and Engineering Geoscience, **15**, 29-40.

Silva, M.R.D., Schroeder, C. & Verbrugge, J. 2008. Unsaturated rock mechanics applied to a low-porosity shale. Engineering Geology, **97**, 42-52.

Tang, S.B., Yu, C.Y., Heap, M.J., Chen, P.Z. & Ren, Y.G. 2018. The Influence of Water Saturation on the Short- and Long-Term Mechanical Behavior of Red Sandstone. Rock Mechanics and Rock Engineering, **51**, 2669-2687, doi: 10.1007/s00603-018-1492-3.

Taud, H., Martinez-Angeles, R., Parrot, J. & Hernandez-Escobedo, L. 2005. Porosity estimation method by X-ray computed tomography. Journal of Petroleum Science and Engineering, **47**, 209-217.

Tokunaga, T.K. & Wan, J. 1997. Water film flow along fracture surfaces of porous rock. Water Resources Research, **33**, 1287-1295.

Tsai, T. & Wang, J. 2011. Examination of influences of rainfall patterns on shallow landslides due to dissipation of matric suction. Environmental Earth Sciences, **63**, 65-75.

Tsang, C.F., Neretnieks, I. & Tsang, Y. 2015. Hydrologic issues associated with nuclear waste repositories. Water Resources Research, **51**, 6923-6972.

Van Genuchten, M.T. 1980. A closed-form equation for predicting the hydraulic conductivity of unsaturated soils. Soil science society of America journal, **44**, 892-898.

Vásárhelyi, B. 2003. Some observations regarding the strength and deformability of sandstones in dry and saturated conditions. Bulletin of Engineering Geology and the Environment, **62**, 245-249.

Vásárhelyi, B. & Ván, P. 2006. Influence of water content on the strength of rock. Engineering Geology, **84**, 70-74.

Wang, X. & Cai, M. 2018. Modeling of brittle rock failure considering inter- and intra-grain contact failures. Computers and Geotechnics, **101**, 224-244, doi: 10.1016/j.compgeo.2018.04.016.

Wardlaw, N.C., Li, Y. & Forbes, D. 1987. Pore-throat size correlation from capillary pressure curves. Transport in porous media, **2**, 597-614.

West, G. 1994. Effect of suction on the strength of rock. Quarterly Journal of Engineering Geology and Hydrogeology, **27**, 51-56.

Wong, L.N.Y., Maruvanchery, V. & Liu, G. 2016. Water effects on rock strength and stiffness degradation. Acta Geotechnica, **11**, 713-737.

Wu, Y.S. & Pan, L.H. 2003. Special relative permeability functions with analytical solutions for transient flow into unsaturated rock matrix. Water Resources Research, **39**.

Yang, K.H., Uzuoka, R., Lin, G.L. & Nakai, Y. 2017. Coupled hydro-mechanical analysis of two unstable unsaturated

slopes subject to rainfall infiltration. Engineering Geology, **216**, 13-30.

Zeng, Q., Wang, Y. & Li, K. 2013. Uniform model for moisture transport in porous materials and its application to concrete at selected Chinese regions. Journal of Materials in Civil Engineering, **26**, 05014001.

Zhang, P., Wittmann, F.H., Zhao, T.-j., Lehmann, E.H. & Vontobel, P. 2011. Neutron radiography, a powerful method to determine time-dependent moisture distributions in concrete. Nuclear Engineering and Design, **241**, 4758-4766.

Zhang, X., Sanderson, D.J. & Barker, A.J. 2002. Numerical study of fluid flow of deforming fractured rocks using dual permeability model. Geophysical Journal International, **151**, 452-468.

Zhao, Y., Wu, Y., Han, S., Xue, S., Fan, G., Chen, Z. & Abd, A.E. 2019. Water sorptivity of unsaturated fractured sandstone: Fractal modeling and neutron radiography experiment. Advances in Water Resources, **130**, 172-183.

Zhao, Y., Xue, S., Han, S., Chen, Z., Liu, S., Elsworth, D., He, L., Cai, J., Liu, Y. & Chen, D. 2017. Effects of microstructure on water imbibition in sandstones using X‐ray computed tomography and neutron radiography. Journal of Geophysical Research: Solid Earth, **122**, 4963-4981.

Zhao, Y., Xue, S., Han, S., He, L. & Chen, Z. 2018. Characterization of unsaturated diffusivity of tight sandstones using neutron radiography. International Journal of Heat and Mass Transfer, **124**, 693-705.

Zhou, Z., Cai, X., Cao, W., Li, X. & Xiong, C. 2016. Influence of water content on mechanical properties of rock in both saturation and drying processes. Rock Mechanics and Rock Engineering, **49**, 3009-3025.

728 **List of Tables**

729 **Table 1** Saturation states of specimens with increasing soaking time.

| Time /min | Weight /g | | |
|---|---|---|---|
| | SZ-01 | SZ-02 | SZ-03 |
| 0 | 415.88 | 416.35 | 416.07 |
| 1 | 424.64 | 425.52 | 426.35 |
| 2 | 427.36 | 428.99 | 429.61 |
| 3 | 428.81 | 430.11 | 430.30 |
| 4 | 430.30 | 432.01 | 433.42 |
| 6 | 431.86 | 432.80 | 435.06 |
| 8 | 433.06 | 433.66 | 435.25 |
| 10 | 433.75 | 433.99 | 435.24 |
| 12 | 433.91 | 433.99 | 435.29 |
| 14 | 433.96 | 434.01 | 435.30 |
| 16 | 433.89 | 434.08 | 435.30 |
| 18 | 433.95 | 434.05 | 435.34 |
| 20 | 433.97 | 434.08 | 435.34 |

730

731 **Table 2** The mesoscale physical properties used to study the mechanical behavior of saturated sandstone (found
732 through calibration). $E$ – Young's (elastic) modulus; $\upsilon$ – Poisson's ratio; $K_n$ – normal stiffness of the sub-contact;
733 $K_s$ – shear stiffness of the sub-contact; $J_T$ – tensile strength of the sub-contact; $J_c$ – cohesion of the sub-contact;
734 $\varphi$ – friction angle of the sub-contact; $\varphi_r$ – residual friction angle of the sub-contact.

| $E$ /GPa | $v$ | $K_n$/GPa·mm$^{-1}$ | $K_n/K_s$ | $J_T$ /MPa | $J_c$ /MPa | $\varphi$/° | $\varphi_r$ /° |
|---|---|---|---|---|---|---|---|
| 9.5 | 0.27 | 40 | 2 | 2.16 | 6.1 | 27 | 6 |

735
736

**List of figure captions**

**Fig. 1** Schematic of the induction of an NMR signal. (a) Natural state. (b) Equilibrium state. (c) Excited state. (d) Spin relaxation state.

**Fig. 2** (a) Location of the six radial water imbibition profiles in the specimen (left). (b) Typical water content profiles for distilled water imbibition along the six monitoring lines (the radial green line in the left) in specimen at 180 s.

**Fig. 3** NMR image of sandstone specimen after soaking times of 180 s (left) and the corresponding NMR image processed by the MATLAB software packages (right).

**Fig. 4** NMR images of water imbibition into rock specimens after different soaking time durations, showing the wetted zone and wet front.

**Fig. 5** (a) Water content profiles measured by NMR during the imbibition of water in Yunnan sandstone. (b) Boltzmann transformation of the measured water content profiles for Yunnan sandstone. (c) The wetting front as a function of the square root of time (t) for the sandstone specimens. (d) The unsaturated hydraulic diffusivity shown in log scale units as a function of the volumetric water content.

**Fig. 6** Volumetric water content as a function of time at different positions (identified by different colors). The volumetric water contents were measured along the radial line #1 in the specimen (see Fig. 2).

**Fig. 7** Volumetric water content as a function of distance in sandstone samples with constant water content corresponding to saturation degree 49.3% (soaking time 180 s) and standing durations of 120, 240, 480, 720, 960, 1200, 1440, and 1680 s.

**Fig. 8** (a) NMR images of the samples soaked for different durations (30, 90, and 180 s) following soaking for 90 s. (b) NMR images of the samples soaked for 120, 180, and 270 s. (c) Water content profiles measured by NMR during the imbibition of water into the samples.

**Fig. 9** (a) Three dimensional Voronoi tessellation designed to replicate the grain scale properties of the sandstone. (b) Scanning electron microscope (SEM) image of Yunnan sandstone.

**Fig. 10** (a) Casting thin section of Yunnan sandstone. The dark blue part is casting, and the mineral grains are bonded and the moisture transport is through grain boundaries or pores. (b) Smooth parallel-plate model on grain contacts where sub-contacts correspond to parallel-plate subregions containing solid-solid contact points and pore space whose aperture is a constant value. (c) Probability distribution of pore diameters in the studied sandstone. The black and red curves are the test and fitting curves, respectively.

766 **Fig. 11** Numerical results of the volumetric water content distribution during capillary imbibition for soaking
767 durations of 30, 90, 180, 300, 480, 720, and 1200 s.
768 **Fig. 12** Numerical results of the volumetric water content distribution in sandstone with constant water content
769 corresponding to saturation degree 49.3% (soaking time 180 s) and standing durations of 120, 240, 480, 720, 960,
770 1200, 1440, and 1680 s.
771 **Fig. 13** Simulated uniaxial stress-strain curves (solid curves) for the numerical samples with different levels of
772 saturation (from 13.1% to 100%) plotted alongside the experimental uniaxial stress-strain curves (dashed curves)
773 for Yunnan sandstone with different levels of saturation (from 13.1% to 100%).
774 **Fig. 14** Variations of macro mechanical properties (compressive strength, direct tensile strength, and Young's
775 modulus) as a function of standing duration. Axial stress for the specimen is measured here as the z-direction
776 forces on the top surface divided by the cross-sectional area of the sample.
777 **Fig. 15** Measurement of axial stress for the specimens with constant water content, but different standing durations.
778 (a) Axial stress for the specimen is measured as the mean axial stress recorded in the red zones (20 mm × 20 mm
779 × 40 mm). (b) The five box sizes investigated for axial stress measurement of the specimen with standing duration
780 of 120 s.
781 **Fig. 16** (a) Uniaxial compressive strength as a function of water saturation for Yunnan sandstone. The red points
782 represent the experimental data and the blue points represent strength predictions for Yunnan sandstone based on
783 the empirical relationships presented in Shakoor and Barefield (2009). (b) Relative uniaxial compressive strength
784 as a function of water saturation. The blue points are data from Demarco et al. (2007) for a range of sandstones
785 and the red points are data for Yunnan sandstone (data from this study).
786

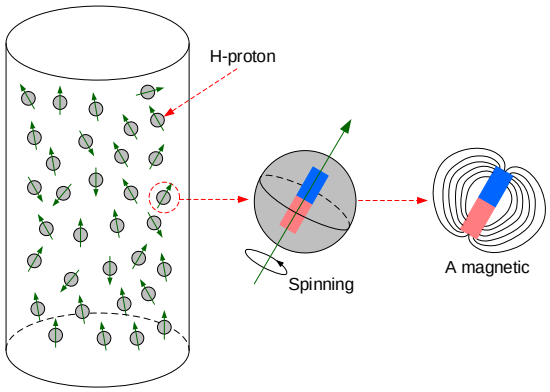


787

788 (a)

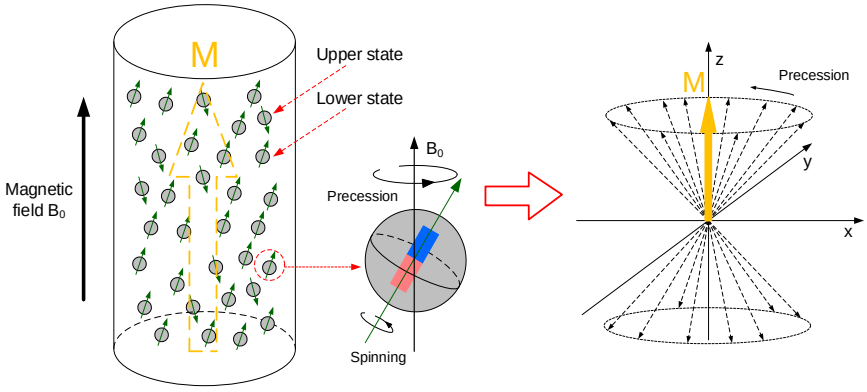


789

790 (b)

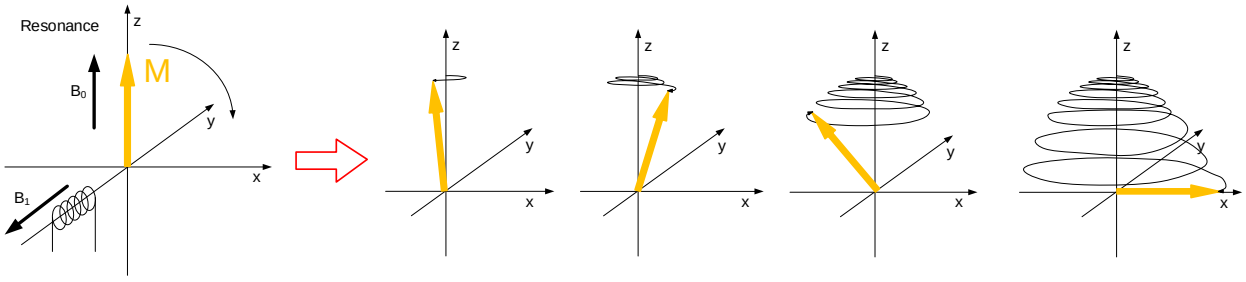


791

792

793 (c)

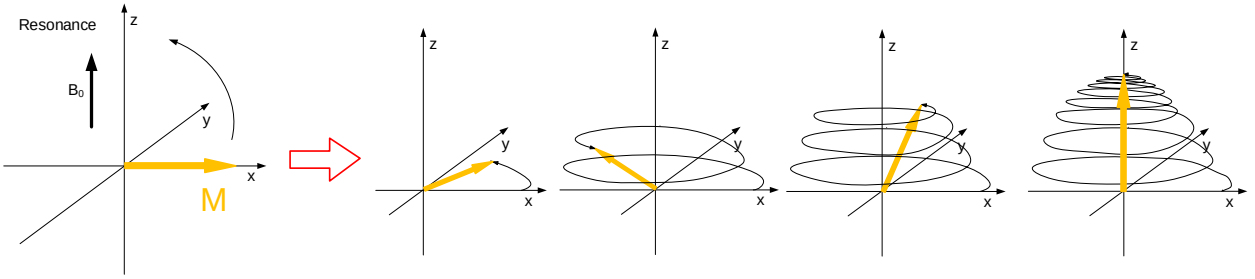


794

795

796 (d)

797 Fig. 1

798

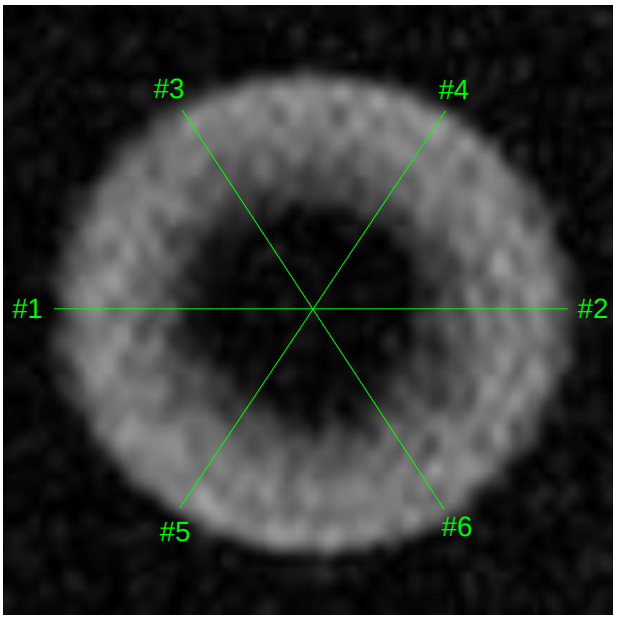
#3
#4
#1
#2
#5
#6

(a)

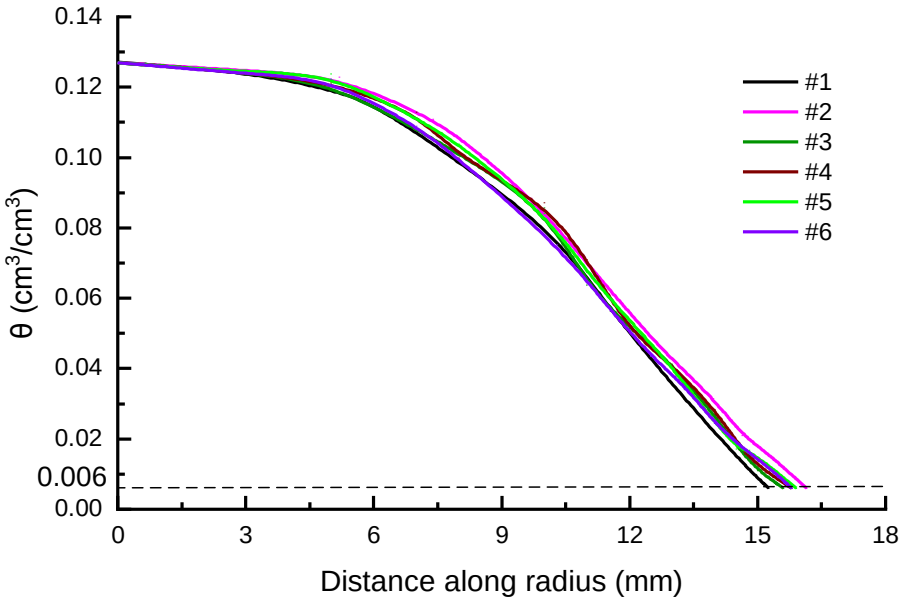
0.14
0.12
0.10
0.08
0.06
0.04
0.02
0.006
0.00
θ (cm³/cm³)
0
3
6
9
12
15
18
Distance along radius (mm)
#1
#2
#3
#4
#5
#6

(b)

Fig. 2

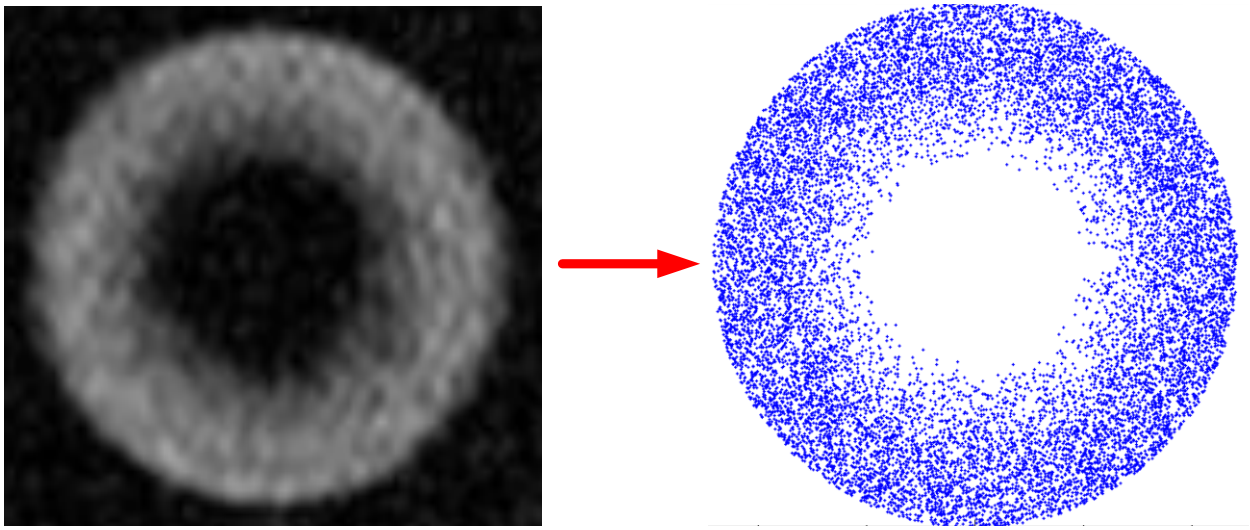

Fig. 3

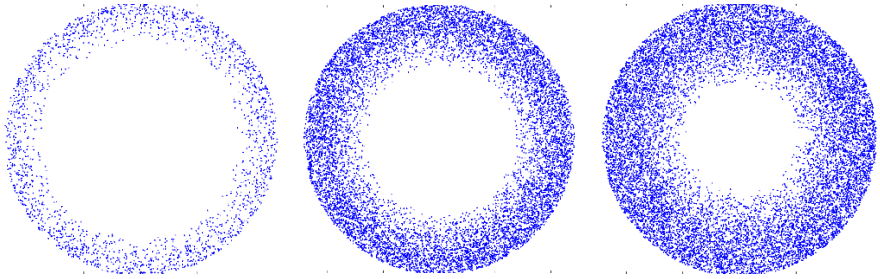

(a) 30 s （b）90 s (c) 180 s

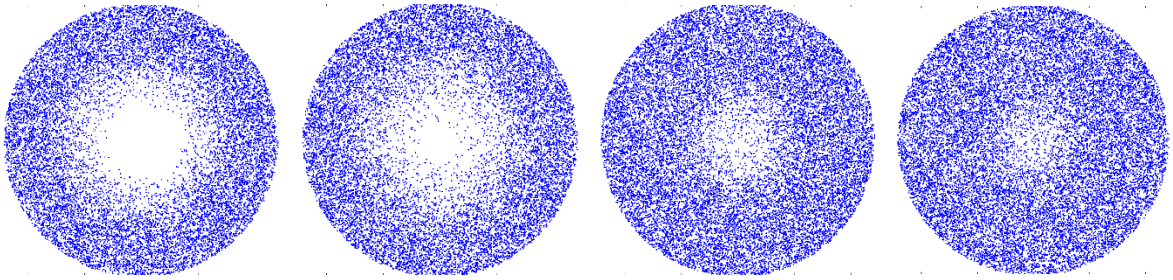

(d) 300 s (e) 480 s (f) 720 s (g) 1200 s

Fig. 4

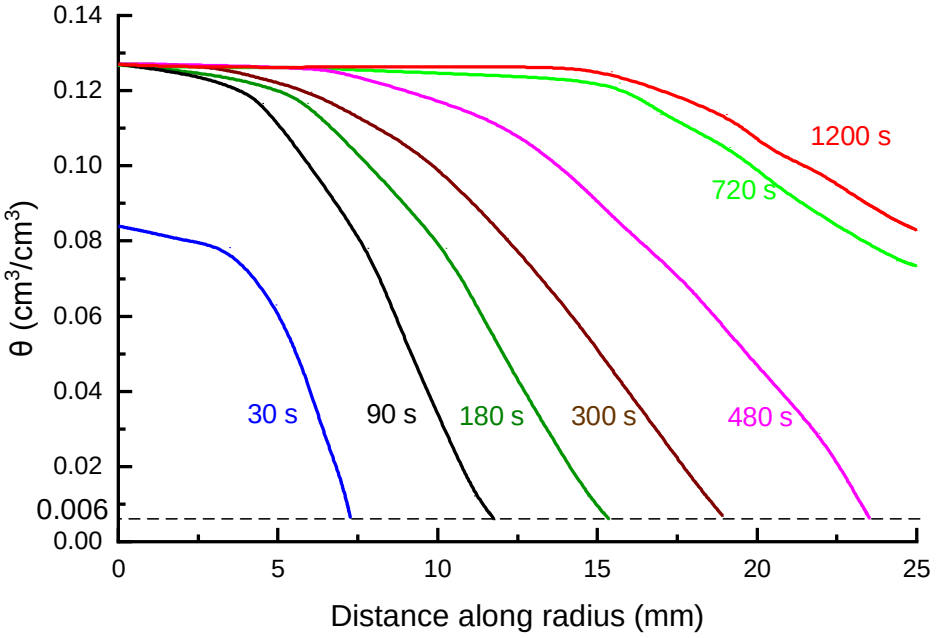
0.14
0.12
0.10
0.08
0.06
0.04
0.02
0.006
0.00
θ (cm³/cm³)
0
5
10
15
20
25
Distance along radius (mm)
1200 s
720 s
480 s
300 s
180 s
90 s
30 s

(a)

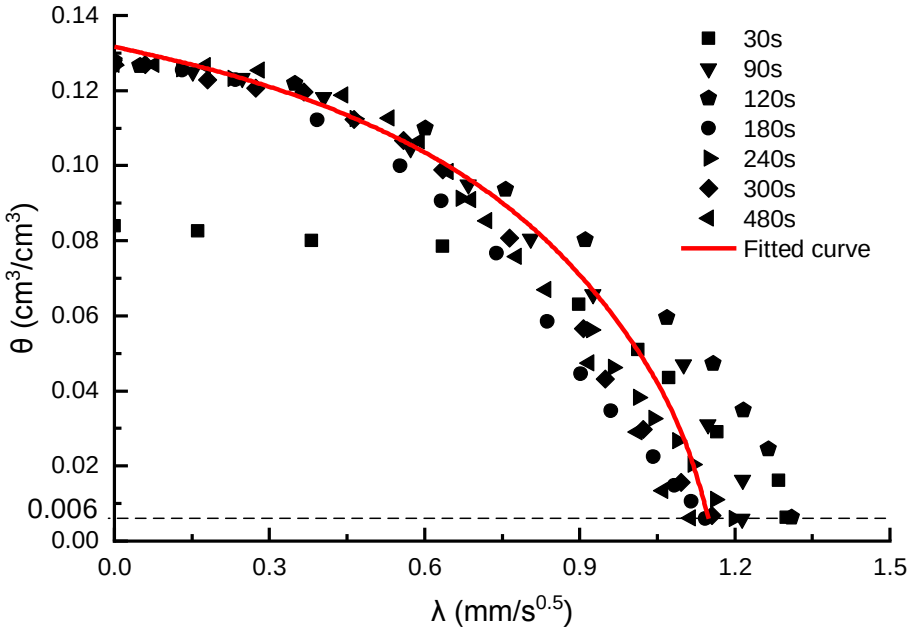
0.14
0.12
0.10
0.08
0.06
0.04
0.02
0.006
0.00
θ (cm³/cm³)
0.0
0.3
0.6
0.9
1.2
1.5
λ (mm/s^0.5)
30s
90s
120s
180s
240s
300s
480s
Fitted curve

(b)

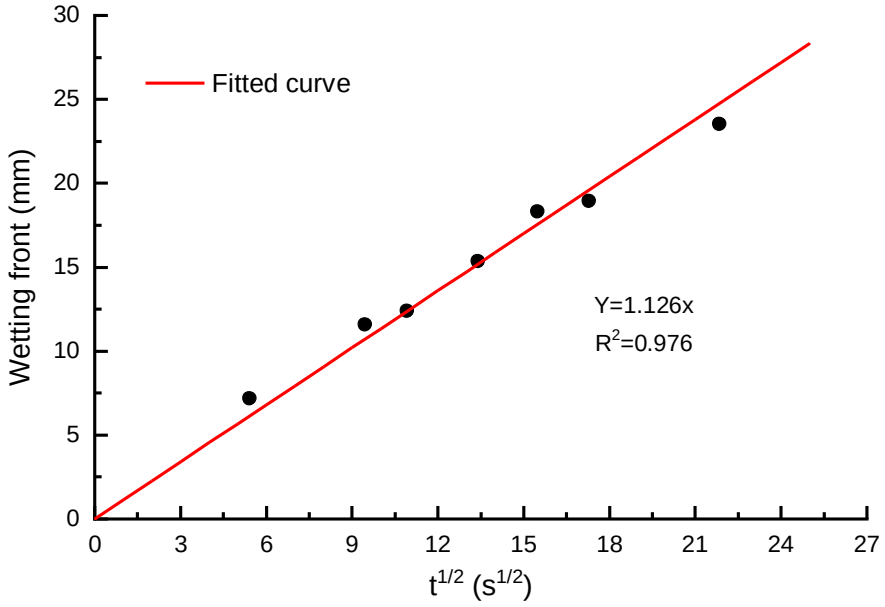


820

821 (c)

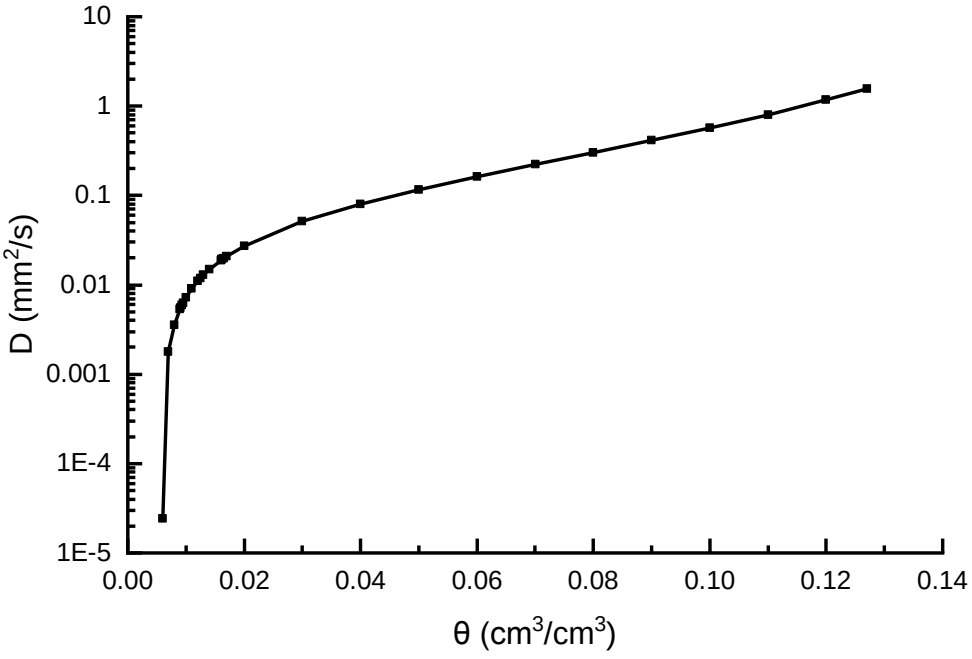


822

823 (d)

824 Fig. 5

825

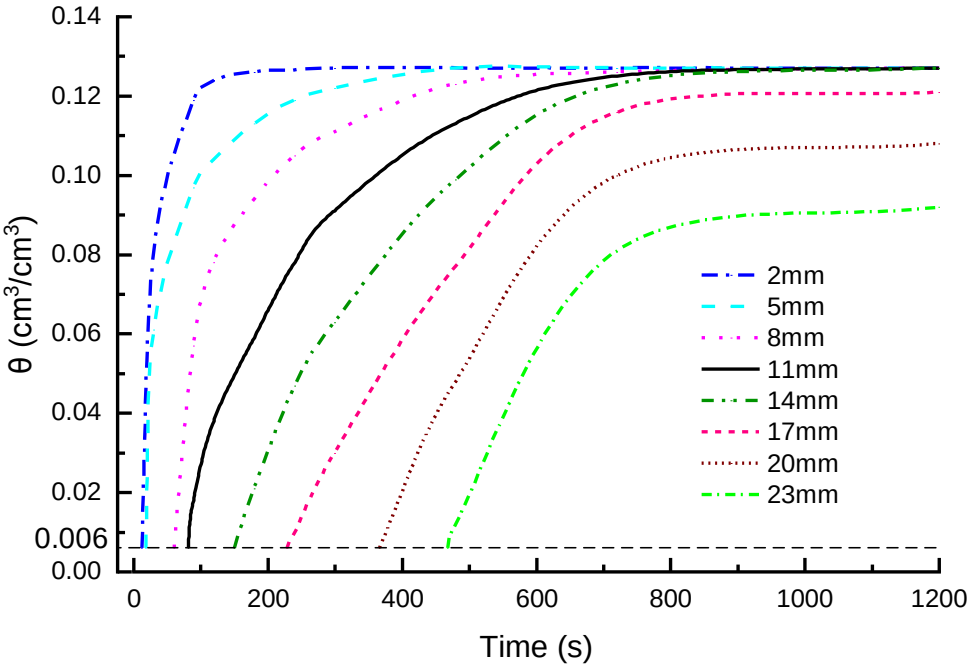


826

827 Fig. 6

828

829

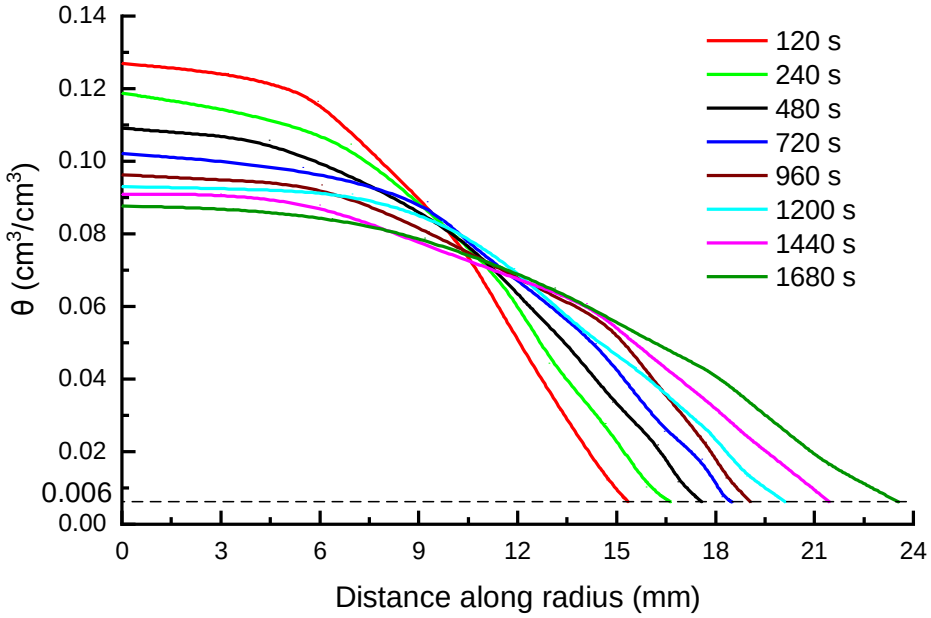
0.14
0.12
0.10
0.08
0.06
0.04
0.02
0.006
0.00
θ (cm³/cm³)
0
3
6
9
12
15
18
21
24
Distance along radius (mm)
120 s
240 s
480 s
720 s
960 s
1200 s
1440 s
1680 s

Fig. 7

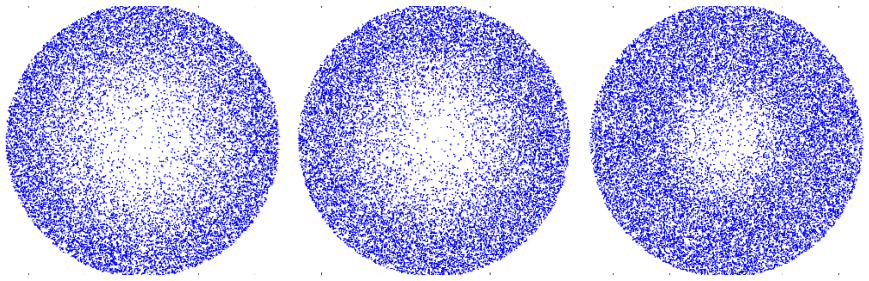

(a)

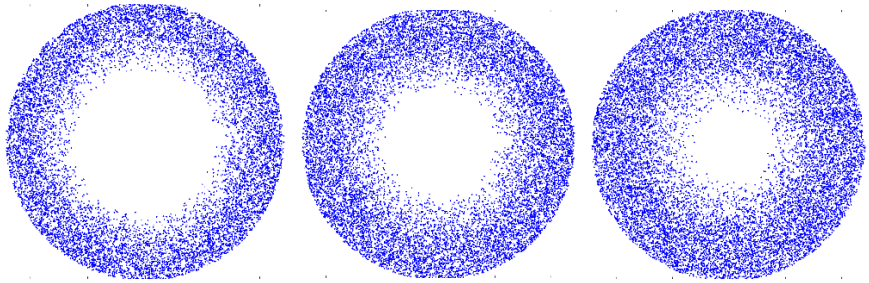

(b)

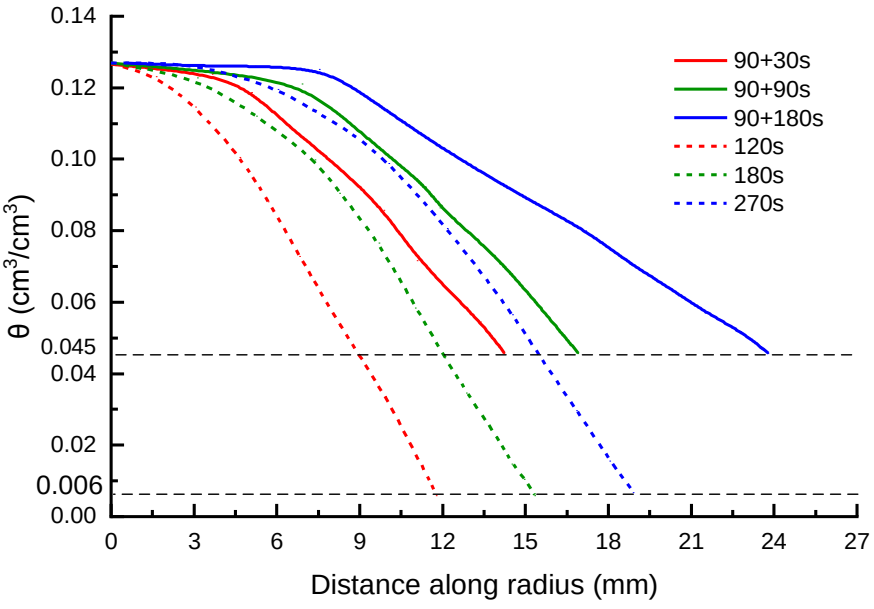
0.14
0.12
0.10
0.08
0.06
0.045
0.04
0.02
0.006
0.00
θ (cm³/cm³)
0
3
6
9
12
15
18
21
24
27
Distance along radius (mm)
90+30s
90+90s
90+180s
120s
180s
270s

(c)

Fig. 8

841

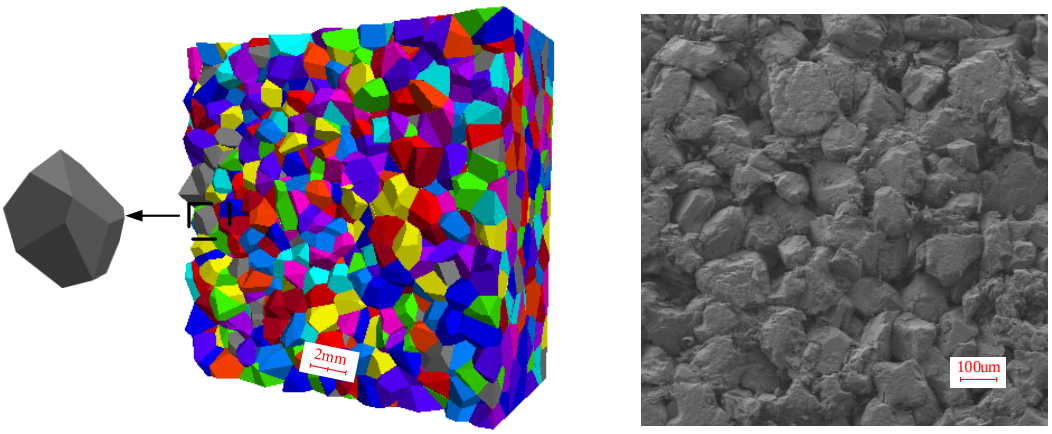


842 (a) (b)

843 Fig. 9

844

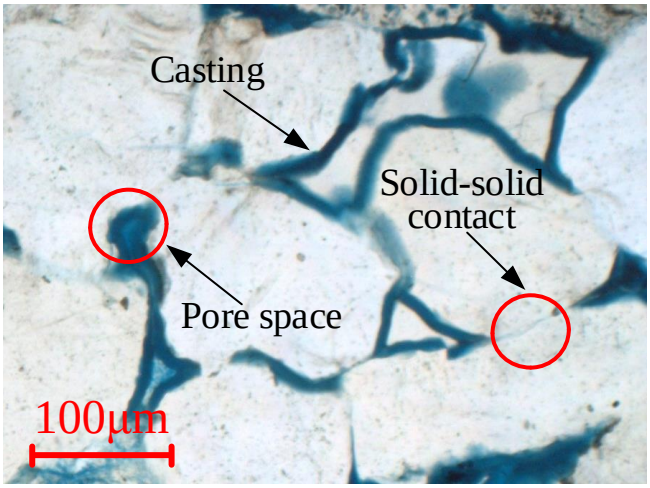


845

846 (a)

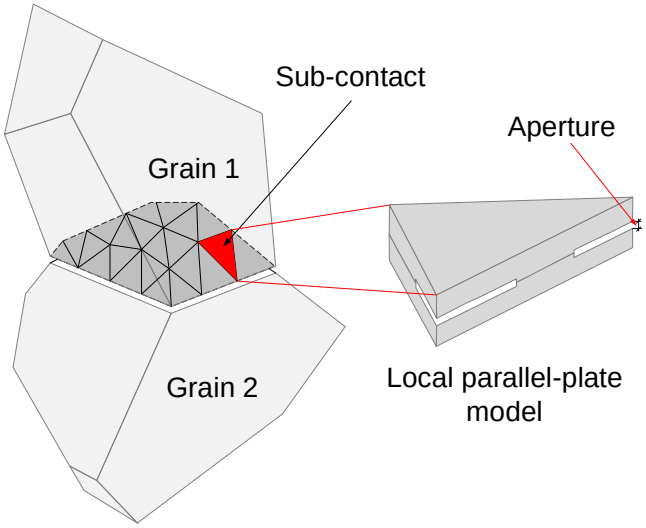


847

848 (b)

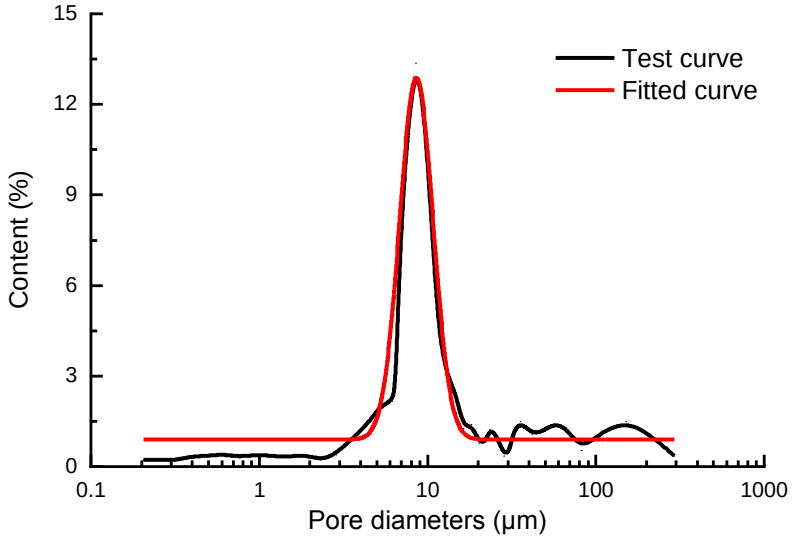


849

850 (c)

851 Fig. 10

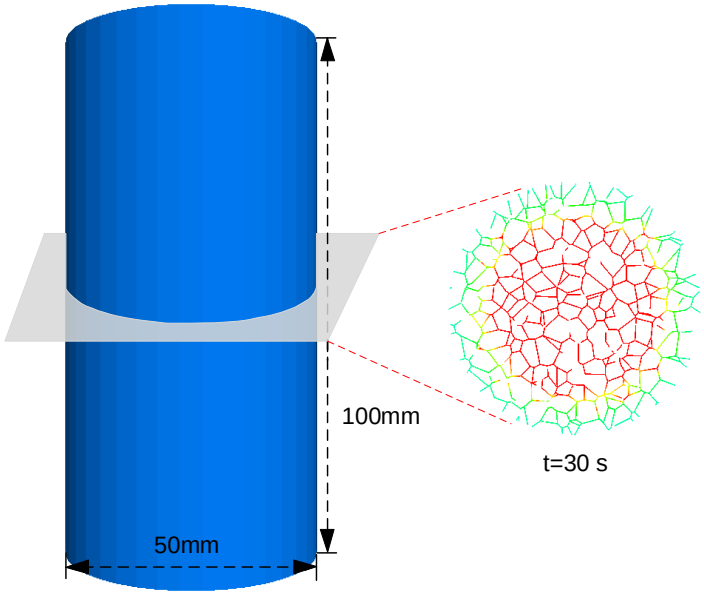


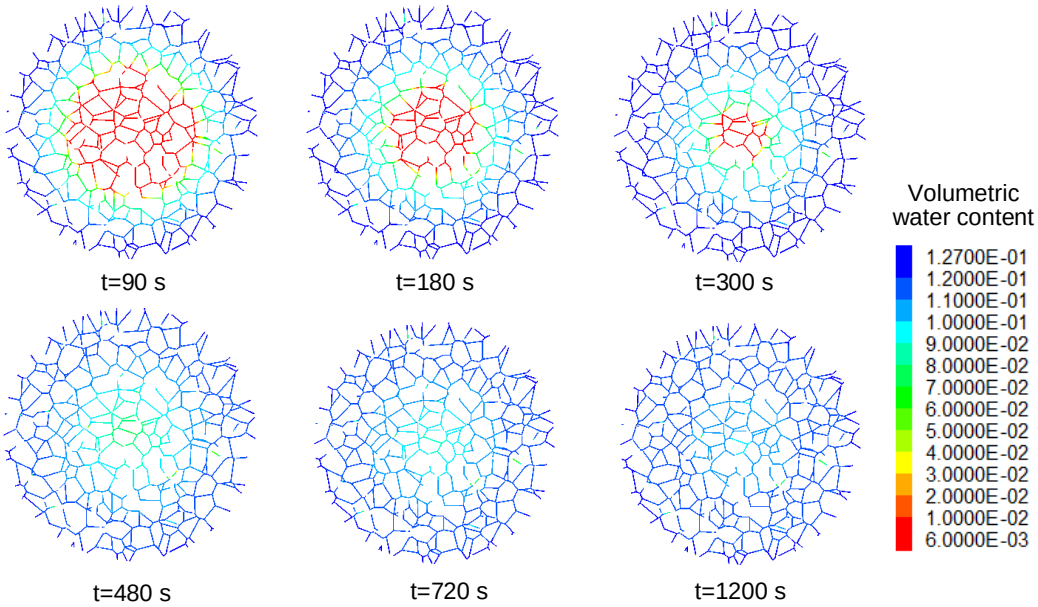


852

853 Fig. 11

854

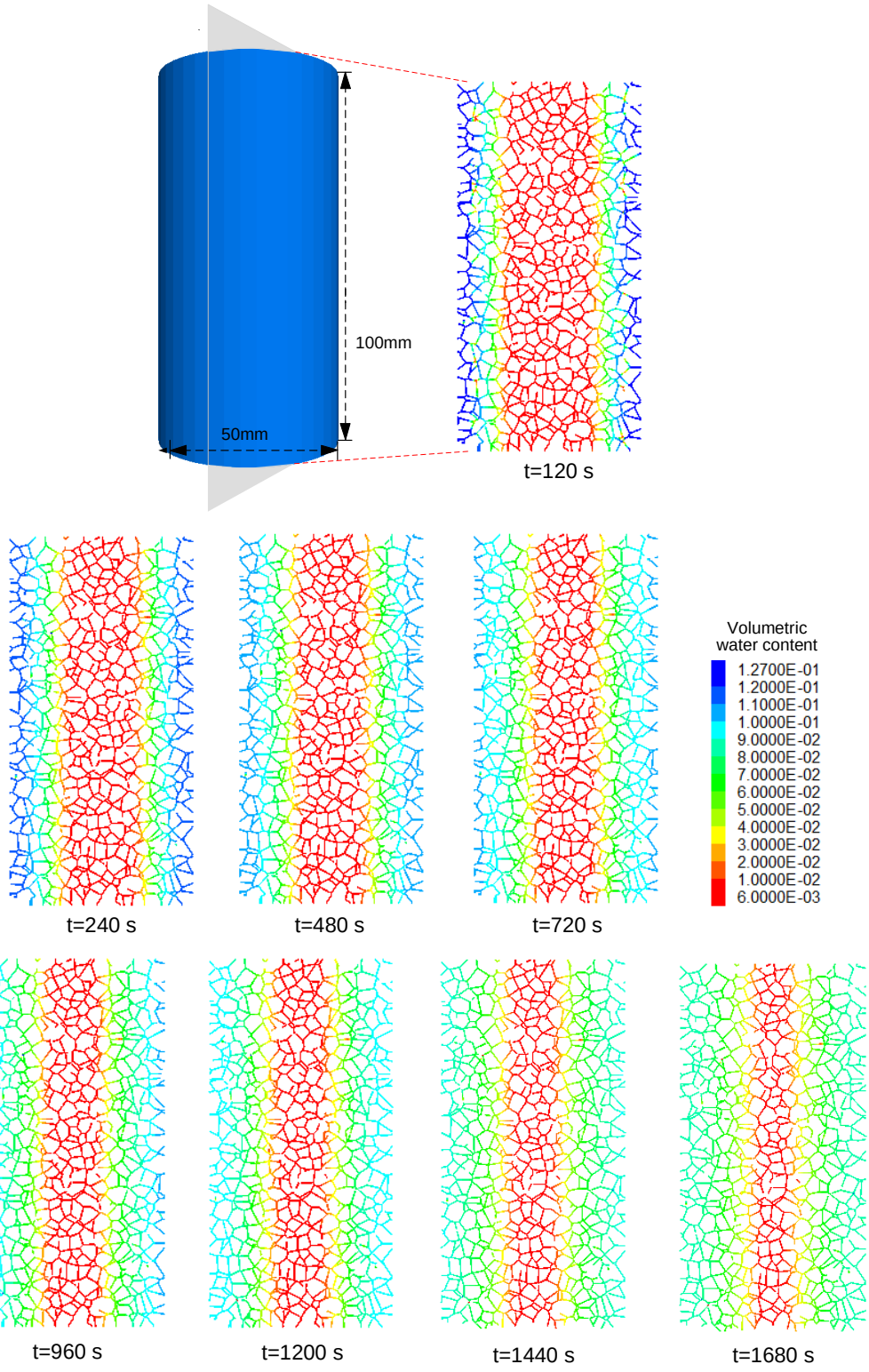
100mm
50mm
t=120 s
t=240 s
t=480 s
t=720 s
Volumetric water content
1.2700E-01
1.2000E-01
1.1000E-01
1.0000E-01
9.0000E-02
8.0000E-02
7.0000E-02
6.0000E-02
5.0000E-02
4.0000E-02
3.0000E-02
2.0000E-02
1.0000E-02
6.0000E-03
t=960 s
t=1200 s
t=1440 s
t=1680 s

Fig. 12

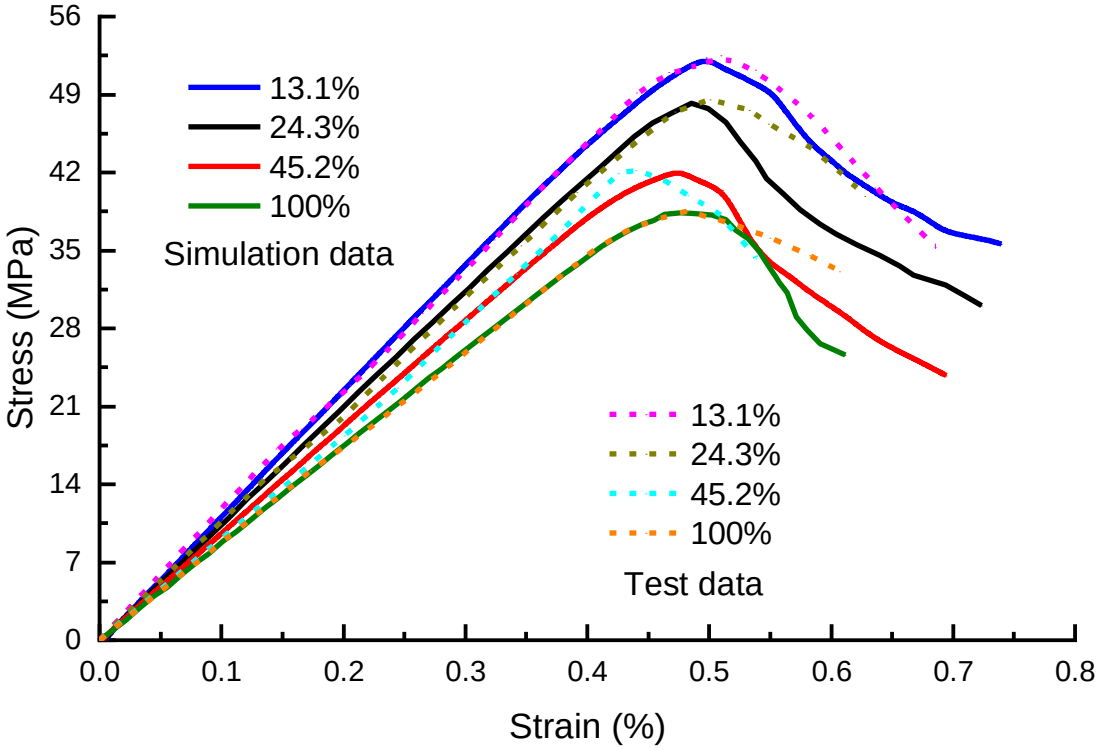


858

859 Fig. 13

860

861

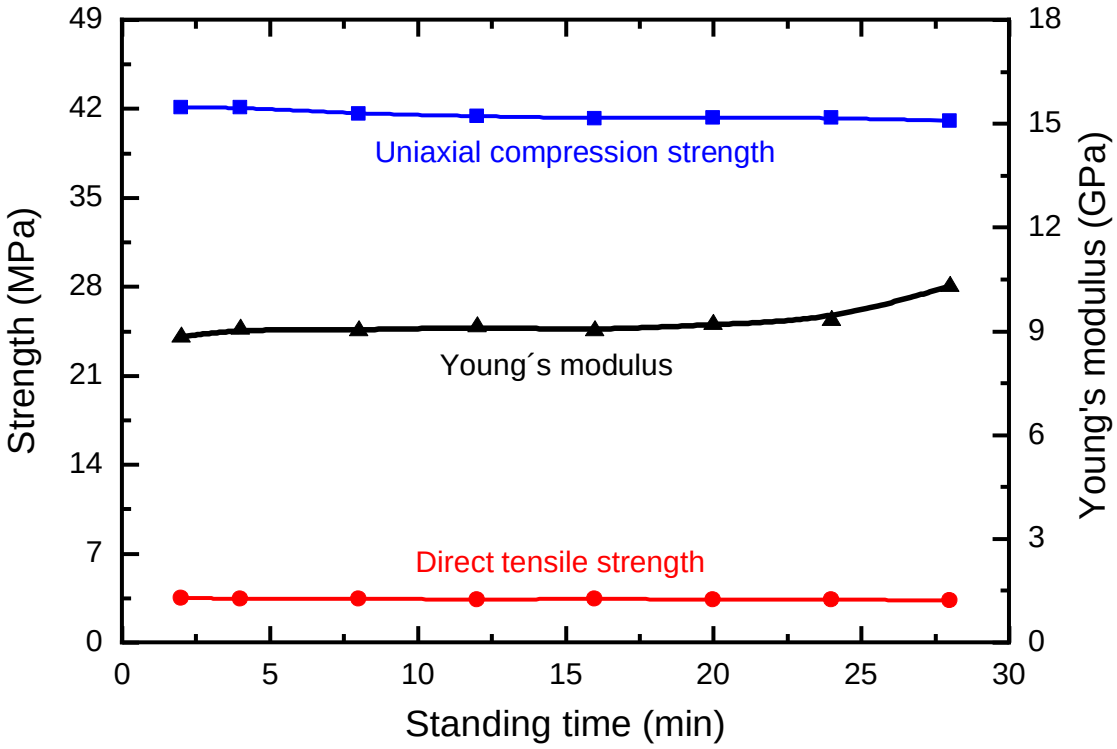


862

863 Fig. 14

864

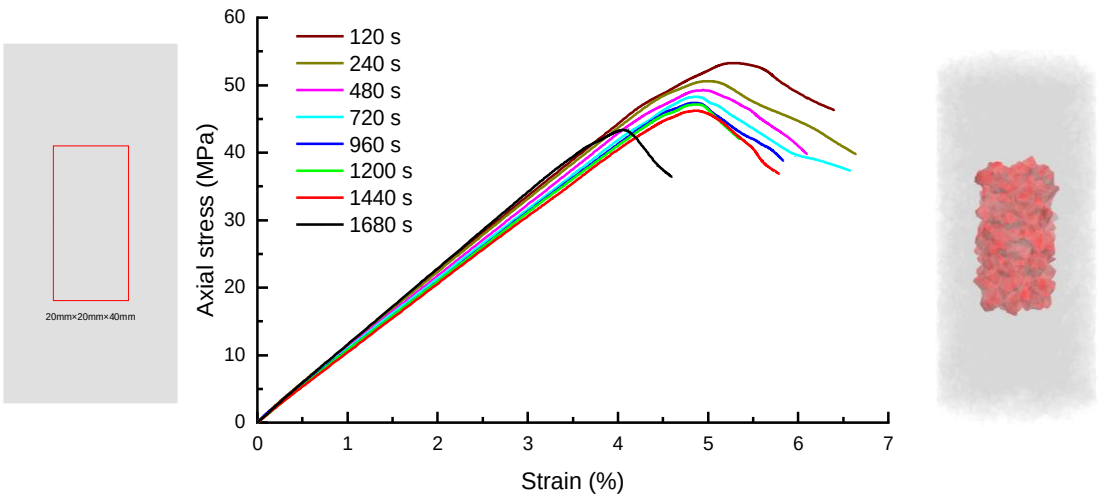
20mm×20mm×40mm
120 s
240 s
480 s
720 s
960 s
1200 s
1440 s
1680 s
Axial stress (MPa)
Strain (%)
0
10
20
30
40
50
60
0
1
2
3
4
5
6
7

(a)

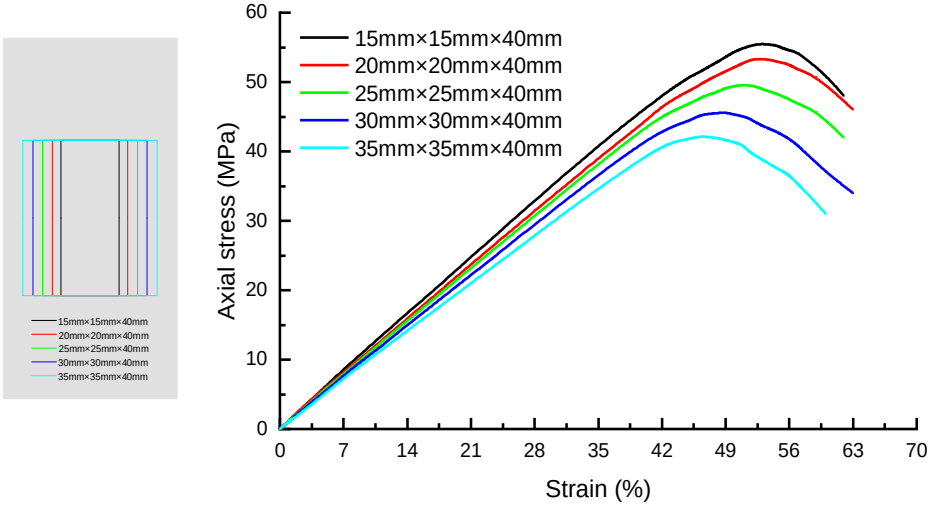
15mm×15mm×40mm
20mm×20mm×40mm
25mm×25mm×40mm
30mm×30mm×40mm
35mm×35mm×40mm
Axial stress (MPa)
Strain (%)
0
10
20
30
40
50
60
0
7
14
21
28
35
42
49
56
63
70

(b)

Fig. 15

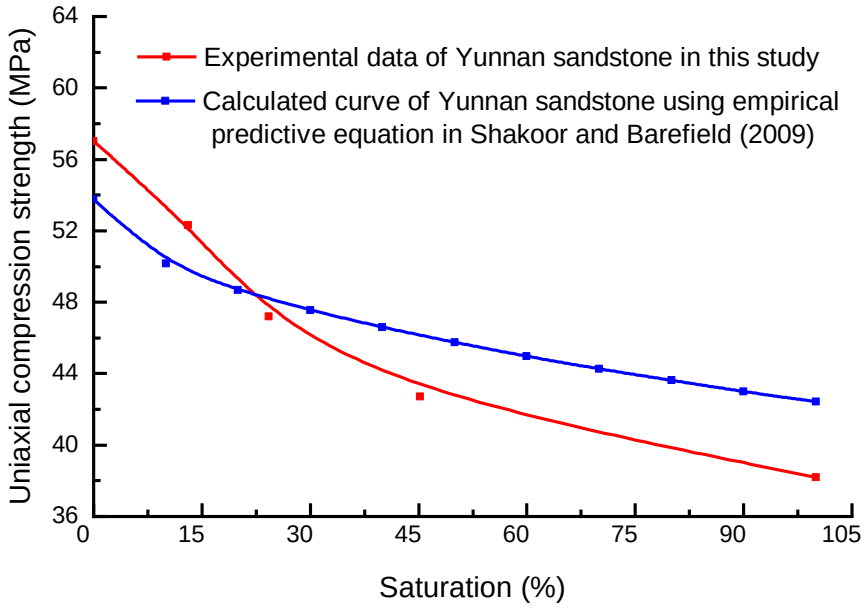


873

874 (a)

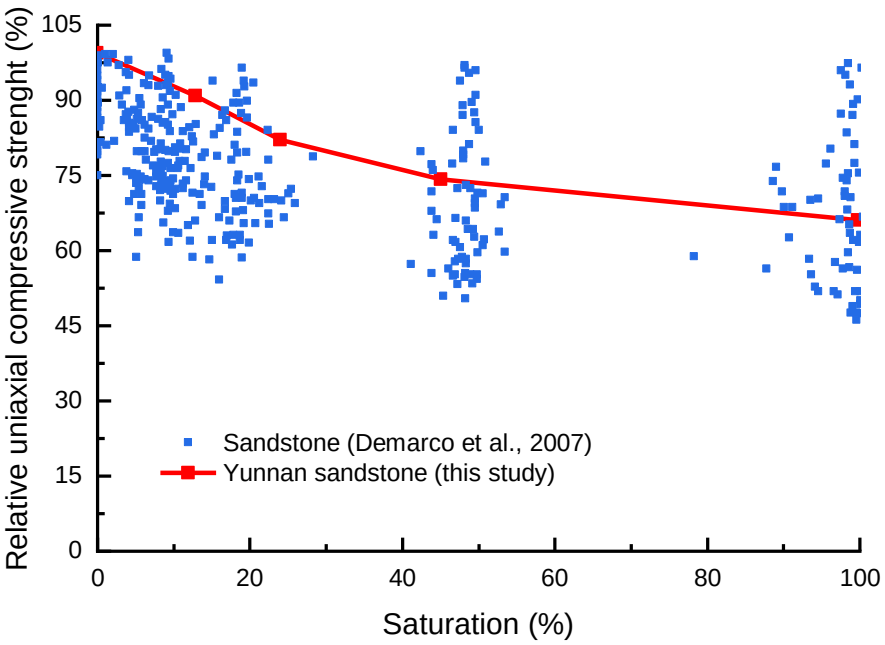


875

876 (b)

877 Fig. 16

878